



**HAL**  
open science

## **Impact of small-scale saline tracer heterogeneity on electrical resistivity monitoring in fully and partially saturated porous media: insights from geoelectrical milli-fluidic experiments**

Damien Jougnot, Joaquín Jiménez-Martínez, Raphaël Legendre, Tanguy Le Borgne, Yves Méheust, Niklas Linde

### ► To cite this version:

Damien Jougnot, Joaquín Jiménez-Martínez, Raphaël Legendre, Tanguy Le Borgne, Yves Méheust, et al.. Impact of small-scale saline tracer heterogeneity on electrical resistivity monitoring in fully and partially saturated porous media: insights from geoelectrical milli-fluidic experiments. *Advances in Water Resources*, 2018, 113, pp.295-309. 10.1016/j.advwatres.2018.01.014 . insu-01686249

**HAL Id: insu-01686249**

**<https://insu.hal.science/insu-01686249>**

Submitted on 17 Jan 2018

**HAL** is a multi-disciplinary open access archive for the deposit and dissemination of scientific research documents, whether they are published or not. The documents may come from teaching and research institutions in France or abroad, or from public or private research centers.

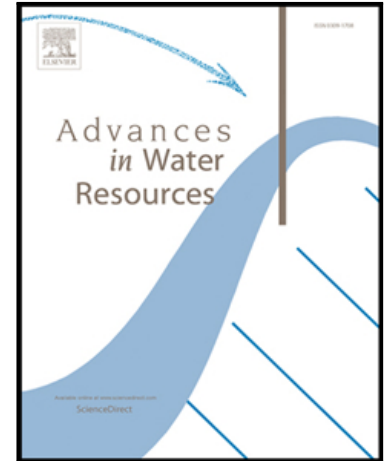
L'archive ouverte pluridisciplinaire **HAL**, est destinée au dépôt et à la diffusion de documents scientifiques de niveau recherche, publiés ou non, émanant des établissements d'enseignement et de recherche français ou étrangers, des laboratoires publics ou privés.

## Accepted Manuscript

Impact of small-scale saline tracer heterogeneity on electrical resistivity monitoring in fully and partially saturated porous media: insights from geoelectrical milli-fluidic experiments

Damien Jougnot, Joaquín Jiménez-Martínez, Raphaël Legendre, Tanguy Le Borgne, Yves Méheust, Niklas Linde

PII: S0309-1708(17)30700-5  
DOI: [10.1016/j.advwatres.2018.01.014](https://doi.org/10.1016/j.advwatres.2018.01.014)  
Reference: ADWR 3070



To appear in: *Advances in Water Resources*

Received date: 13 July 2017  
Revised date: 12 January 2018  
Accepted date: 15 January 2018

Please cite this article as: Damien Jougnot, Joaquín Jiménez-Martínez, Raphaël Legendre, Tanguy Le Borgne, Yves Méheust, Niklas Linde, Impact of small-scale saline tracer heterogeneity on electrical resistivity monitoring in fully and partially saturated porous media: insights from geoelectrical milli-fluidic experiments, *Advances in Water Resources* (2018), doi: [10.1016/j.advwatres.2018.01.014](https://doi.org/10.1016/j.advwatres.2018.01.014)

This is a PDF file of an unedited manuscript that has been accepted for publication. As a service to our customers we are providing this early version of the manuscript. The manuscript will undergo copyediting, typesetting, and review of the resulting proof before it is published in its final form. Please note that during the production process errors may be discovered which could affect the content, and all legal disclaimers that apply to the journal pertain.

Impact of small-scale saline tracer heterogeneity on  
electrical resistivity monitoring in fully and partially  
saturated porous media: insights from geoelectrical  
milli-fluidic experiments

Damien Jougnot<sup>1</sup>

*Sorbonne Universités, UPMC Université Paris 06, CNRS, EPHE, UMR 7619 METIS,  
Paris, France.*

Joaquín Jiménez-Martínez

*Department Water Resources and Drinking Water, Swiss Federal Institute of Aquatic  
Science and Technology, EAWAG, Dübendorf, Switzerland.*

*Department of Civil, Environmental and Geomatic Engineering, ETH Zurich, Zurich,  
Switzerland.*

Raphaël Legendre, Tanguy Le Borgne and Yves Méheust

*Géosciences Rennes (UMR CNRS 6118), University of Rennes 1, Rennes, France.*

Niklas Linde

*Applied and Environmental Geophysics Group, Institute of Earth Sciences, University of  
Lausanne, Switzerland.*

---

**Abstract**

Time-lapse electrical resistivity tomography (ERT) is a geophysical method widely used to remotely monitor the migration of electrically-conductive tracers and contaminant plumes in the subsurface. Interpretations of time-lapse ERT inversion results are generally based on the assumption of a homogeneous solute concentration below the resolution limits of the tomogram depicting inferred electrical conductivity variations. We suggest that ignoring small-scale solute concentration variability (i.e., at the sub-resolution scale) is a major reason for the often-observed apparent loss of solute mass in ERT tracer studies. To demonstrate this, we developed a geoelectrical milli-fluidic setup where the bulk

---

<sup>1</sup>Corresponding author: damien.jougnot@upmc.fr

electric conductivity of a 2D analogous porous medium, consisting of cylindrical grains positioned randomly inside a Hele-Shaw cell, is monitored continuously in time while saline tracer tests are performed through the medium under fully and partially saturated conditions. High resolution images of the porous medium are recorded with a camera at regular time intervals, and provide both the spatial distribution of the fluid phases (aqueous solution and air), and the saline solute concentration field (where the solute consists of a mixture of salt and fluorescein, the latter being used as a proxy for the salt concentration). Effective bulk electrical conductivities computed numerically from the measured solute concentration field and the spatial distributions of fluid phases agree well with the measured bulk conductivities. We find that the effective bulk electrical conductivity is highly influenced by the connectivity of high electrical conductivity regions. The spatial distribution of air, saline tracer fingering, and mixing phenomena drive temporal changes in the effective bulk electrical conductivity by creating preferential paths or barriers for electrical current at the pore-scale. The resulting heterogeneities in the solute concentrations lead to strong anisotropy of the effective bulk electrical conductivity, especially for partially saturated conditions. We highlight how these phenomena contribute to the typically large apparent mass loss observed when conducting field-scale time-lapse ERT.

*Keywords:* Hydrogeophysics, Petrophysics, Millifluidics, Electrical Conductivity, Unsaturated Flow, Tracer test, Transport in Porous Media, Anisotropy

---

## 1. Introduction

Geophysical methods are increasingly used in subsurface hydrology. Their main advantages lie in their largely non-invasive nature, their sensitivity to properties of interest, and in that they provide images of the subsurface at a comparatively high spatial resolution [e.g. 1, 2, 3, 4, 5]. A particular emphasis has been given to geophysical methods with responses that depend on the

7 electrical resistivity (or the electrical conductivity, its inverse) because electrical  
8 resistivity is sensitive to sub-surface properties such as: the lithology (porosity,  
9 tortuosity, specific surface area), the presence of fluids in the pore space (water  
10 saturation and its spatial distribution), and the pore fluid chemistry (ionic con-  
11 centrations). The links between physical properties (electrical resistivity) and  
12 hydrological properties and state variables of interest are described by petro-  
13 physical relationships (for literature reviews, see [4, 6] among others).

14 Resistivity methods can be applied to a wide range of scales, from the labo-  
15 ratory (on centimetric samples) to the field (up to several kilometers). Measure-  
16 ments are achieved by driving a known electrical current between an electrode  
17 pair while measuring the resulting voltage between another electrode pair. The  
18 electrical resistivity structure of the subsurface can be inferred by electrical re-  
19 sistivity tomography (ERT), which is an inversion process that uses measured  
20 electrical resistances from multiple current injection and voltage pairs (e.g.,  
21 Binley and Kemna [7]). If the measurement process is repeated in time, it is  
22 possible to perform time-lapse inversion and, thus, to track temporally-varying  
23 processes in the subsurface (e.g. [8]). Time-lapse ERT has been widely applied  
24 under both saturated (e.g., [9, 10, 11]) and partially saturated conditions (e.g.,  
25 [12, 13, 14, 15]) using electrodes placed on the ground or in boreholes.

26 Geophysical data have a limited resolving power, which implies that geo-  
27 physical tomograms are best understood as spatially-filtered representations of  
28 subsurface properties (e.g., Menke [16], Friedel [17]). The “filter width” is often  
29 referred to as the resolution and it varies in space and time as a function of exper-  
30 imental design, noise, the actual electrical conductivity distribution and choices  
31 made when developing or running an inversion algorithm. In ERT studies, the  
32 resolution decreases (the filter width increases) when the distance between the  
33 electrodes and the target of interest increase. Day-Lewis et al. [18] highlight  
34 the inherent resolution limitations of cross-borehole ERT through a careful nu-  
35 merical and theoretical study. The limited resolution of ERT tomograms can (if  
36 ignored) lead to important errors when translating inferred resistivity to prop-  
37 erties of interest through petrophysical relationships (e.g., [19, 14, 20, 15]). For

38 instance, a common problem is the apparent loss of mass occurring in field-based  
39 experiments when comparing ERT-inferred mass to the actual injected water  
40 volume or mass of salt. For example, Binley et al. [13] noticed an apparent wa-  
41 ter mass loss of 50 % when monitoring a fluid tracer in the vadose zone. Using  
42 a saline tracer in the fully saturated part of an aquifer, Singha and Gorelick [10]  
43 only “recovered” 25% of the mass using ERT data. They demonstrate that this  
44 apparent tracer mass loss is more important when the target volume is small  
45 and the electrical conductivity contrast is high. In a synthetic 3-D time-lapse  
46 study mimicking an actual field experiment, Doetsch et al. [21] obtained a mass  
47 recovery close to 80 %, while the corresponding field experiment provided an  
48 ERT-inferred mass recovery between 10 % and 25 %. The authors attribute this  
49 discrepancy to the fact that classical smoothness-constrained inversions (often  
50 referred to as Occam’s inversion [22]) will, by construction, seek the smoothest  
51 model that fits the data. Due to the upscaling (averaging) process inherent to  
52 electrical current flow, less tracer mass is needed to explain ERT data when a  
53 heterogeneous plume is represented by a larger plume of near-uniform concentra-  
54 tion. Doetsch et al. [21] suggest that this apparent mass loss could potentially  
55 be used as an indicator of the tracer plume heterogeneity at scales below the  
56 resolution of the tomograms. Effects of such small-scale solute concentrations  
57 are commonly ignored and it is implicitly assumed that the solution is perfectly  
58 mixed below this scale. A few studies have considered anomalous transport  
59 and the effect of small-scale heterogeneities on petrophysical relationships (e.g.  
60 [23] [24], [25]). For example, Singha et al. [23], Briggs et al. [26, 27], and  
61 Day-Lewis et al. [28] have proposed dual-domain approaches to account for this  
62 phenomenon.

63 The question of how field-scale studies are impacted by sub-resolution flow  
64 and transport processes is deeply tied to the physics of these processes. For ex-  
65 ample, unsaturated flows give rise to gravitational [29] and viscous [30, 31, 32]  
66 interface instabilities leading to sub-Darcy-scale fingering. It is now well under-  
67 stood that this fingering is the main reason why Darcy-scale modelling of flows  
68 in the unsaturated zone should consider a dependence of the capillary pressure

69 on the local Darcy velocity [33] (the so-called dynamic capillary pressure [34]).  
70 This strong pore-scale heterogeneity of the flow, in particular for unsaturated  
71 flows, is associated with preferential paths for solute transport and incomplete  
72 solute mixing at the pore-scale [35, 36]. Incomplete mixing (e.g. [37, 38]) and  
73 strong heterogeneities of the advection paths for solutes (as observed also at  
74 larger scales (e.g. [39, 40]), result in anomalous transport that makes Fick-  
75 ian models unsuitable at the Darcy scale and at the block scale corresponding  
76 to the grid size used for numerical simulations [36]. Geophysical monitoring  
77 data of solute transport and mixing processes are also likely impacted by such  
78 mechanisms acting at sub-resolution scales.

79 Recent advances in milli- and micro-fluidic laboratory experiments provide  
80 means to better understand and predict pore-scale transport properties and  
81 mixing in saturated (e.g., [41], [42]) and partially saturated porous media (e.g.  
82 [35, 36]). In a pioneering work, Kozlov et al. [43] investigate the validity and  
83 limitations of a classical petrophysical relationship involving electrical conduc-  
84 tivity in a porous micro-model filled by water and oil, but without considering  
85 solute transport. The present work builds on the experimental developments  
86 of Jiménez-Martínez et al. [35, 36] and aims to study the effect of the spa-  
87 tial distribution of phases and solute concentration field on the bulk electrical  
88 resistivity below the ERT resolution. This is the first time a laboratory pore-  
89 scale fluorimetric flow and transport experiment is equipped with geoelectrical  
90 monitoring capabilities.

91 The manuscript is organized as follows: in section 2 we present our geoelec-  
92 trical milli-fluidic experimental setup; we then explain the image treatment and  
93 the numerical modeling of the electrical problem (section 3); finally, we present  
94 and discuss in section 4 the results that we have obtained from tracer tests under  
95 fully-saturated and partially-saturated conditions, and how these results can be  
96 used to gain insights into how upscaled bulk electrical resistivity is affected by  
97 sub-resolution heterogeneity and processes.

## 98 2. Experimental method

### 99 2.1. Milli-fluidic setup for spatially-resolved pore-scale fluorimetry

100 We build on the recent experimental developments by de Anna et al. [42] and  
101 Jiménez-Martínez et al. [35, 36] and consider a 2D analogous porous medium  
102 which we refer to as the flow cell (Fig. 1). Using such a setup, it is possible to  
103 measure the spatial distribution of the fluids in the cell and the ionic concen-  
104 tration field in the liquid (wetting) phase using a fluorimetry technique. A light  
105 source is placed below the cell (Fig. 1a) and the cell is monitored using a high-  
106 resolution camera (27 pixels per mm, 12 bit images), positioned 32 cm above  
107 the flow cell with its axis normal to the horizontal mean plane of the cell. The  
108 light source excites the fluorescent tracer present in the wetting solution; the  
109 tracer consequently emits light around a given wavelength, which is recorded by  
110 the camera. A filter placed on the light source prevents light with wavelengths  
111 belonging to the emission range of fluorescein to go through the flow cell, while  
112 a band-pass filter located in front of the camera allows the light intensity cor-  
113 responding only to the fluorescein excitation to be recorded. We can thus track  
114 the spatial distribution of the fluids (air and water) phases. Furthermore, as the  
115 intensity of the light recorded on a given pixel of the camera sensor depends on  
116 the mean fluorescein concentration probed along the direction between the light  
117 source and the sensor, the spatial distribution of the intensity recorded on an  
118 image provides a measure of the 2D spatial distribution of the fluorescein (or fluo-  
119 rescein concentration field) within the liquid phase. By fixing a concentration  
120 ratio between the fluorescein and another ionic species having a similar diffusion  
121 coefficients (NaCl in this study), it is possible to infer the concentration field  
122 of the salt from that of the fluorescein. For this study, the camera monitoring  
123 system (MegaPlus EP11000, Princeton Instruments) was set to take 1 picture  
124 every 2 s to capture the fluid phases and solute dynamics in the flow cell.

125 The flow cell consists of a single layer of 4500 cylindrical solid grains posi-  
126 tioned between two parallel transparent plates separated by a distance equal to  
127 the cylinders' height. It is built by soft lithography as follow. Two glass plates

128 are separated by the desired distance using spacers. The space between them is  
129 filled with a UV-sensitive polymer (NOA-81). The photomask (resulting from  
130 a numerical model of the 2D compaction of circular grains with diameters dis-  
131 tributed according to a Gaussian law of prescribed standard deviation) is then  
132 placed on top of the top plate. The mask is transparent where solid grains are  
133 to be found, opaque everywhere else. The light coming from the collimated 365  
134 nm UV source passes through the transparent disks in the mask, polymerizing  
135 the NOA-81 and giving rise to solid cylindrical grains spanning the vertical gap  
136 between the two glass plates. The remnant uncured, still liquid, polymer mate-  
137 rial is cleaned by flowing through ethanol. The resulting 2-D porous medium is  
138 water-wet.

139 The geometry used herein corresponds to the so-called homogeneous geom-  
140 etry used by Ferrari et al. [44]. The flow cell is closed on two of its lateral sides  
141 (facing each other), while the two other lateral sides remain open and constitute  
142 the inlet and outlet of the cell. Its length, defined between the inlet and outlet,  
143 is 140 mm, its width is 92 mm, and its thickness (equal to the cylinder height)  
144 is 0.5 mm (see [35] for details). The cell is positioned with the glass plates lying  
145 horizontal. The vertically-oriented cylindrical grains act as obstacles for the  
146 flow of fluids in the cell (Fig. 1a). This 2D geometry has a cross-sectional area  
147 of 43.64 mm<sup>2</sup> in the direction normal to the average flow direction and typical  
148 pore throat and pore sizes of 1.07 mm and 1.75 mm, respectively. It yields a  
149 permeability of  $4.32 \times 10^{-9}$  m<sup>2</sup>.

150 The cell is connected to three reservoirs upstream that contain wetting and  
151 non-wetting fluids, and to an outlet reservoir downstream. The fluids are in-  
152 jected in the flow cell with syringe pumps at a controlled flow rate. The non-  
153 wetting phase is air (Fig. 1a) and the wetting (i.e., liquid) phase is a 60-40 %  
154 by weight distilled water/glycerol solution (see [35]). The glycerol increases  
155 the viscosity of the solution ( $\mu_w = 3.78 \times 10^{-2}$  Pa s), thereby increasing the  
156 viscosity ratio between the wetting and non-wetting phases, and slowing down  
157 molecular diffusion. The wetting phase solutions 1 and 2 have different mass  
158 concentrations of NaCl salt ( $C_{\text{NaCl}}$ ) and fluorescein ( $C_{\text{fluo}}$ ). These solutions are

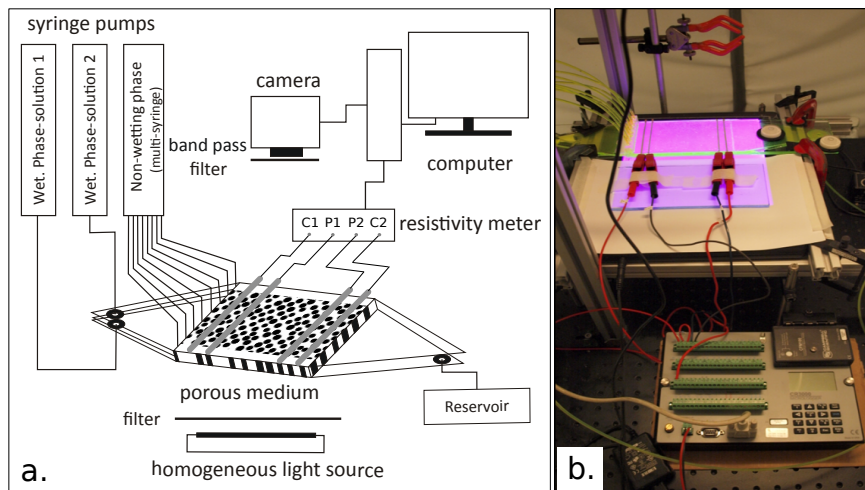


Figure 1: (a) Overall scheme of the setup for the fluorimetric study in the 2D porous medium, featuring the injection systems for air (non-wetting fluid phase), the tracer solution (wetting phase 1), and the background solution (wetting phase 2), as well as the camera and the electrical resistivity monitoring system (modified from [35]). (b) Photography of the geoelectrical milli-fluidic setup.

159 labeled “tracer” (tr) and “background” (bkg) concentrations, respectively. The  
 160 mass concentration of fluorescein is ten times smaller than that of the NaCl salt  
 161 (i.e.,  $C_{\text{NaCl}} = 10 C_{\text{fluo}}$ ).

162 In order to relate the measured light intensity to the electrical conductivity  
 163 of the solution, we first synthesized a set of ten solutions with different  
 164 fluorescein/NaCl salt concentrations by successive dilutions, with  $C_{\text{fluo}}$  rang-  
 165 ing between 701.5 and 0.0856 mg L<sup>-1</sup>. The ratio of NaCl to fluorescein mass  
 166 concentration is identical for all ten solutions and set to 10. The electrical  
 167 conductivity of each solution was measured with a handheld electrical conduc-  
 168 tivity meter (WTW Cond 340i). Correspondingly, the light intensity of each  
 169 solution was measured in a cell similar to the one used for the tracer experi-  
 170 ments (i.e., same glass and aperture thickness) but without cylindrical pillars.  
 171 For the tracer experiments, we chose the background concentration solution  
 172 ( $C_{\text{fluo}}^{\text{tr}} = 5.48 \text{ mg L}^{-1}$ ) by measuring the light intensity for all the solutions and

173 selecting the lowest concentration for which the corresponding light intensity was  
174 above the detection threshold. Then, we chose the tracer concentration to be  
175  $C_{\text{fluo}}^{\text{tr}} = 350.8 \text{ mg L}^{-1}$  in to avoid light saturation for the camera. It yields a back-  
176 ground and tracer electrical conductivity of  $\sigma_{\text{w}}^{\text{bkg}} = 0.0055$  and  $\sigma_{\text{w}}^{\text{tr}} = 0.213 \text{ S m}^{-1}$ ,  
177 respectively. We only kept the six solutions with fluorescein mass concentrations  
178 in between these two values to establish the calibration curve. Combining these  
179 two sets of measurements and using a Piecewise Cubic Hermite Interpolating  
180 Polynomial interpolation in between the data, we obtain an empirical curve re-  
181 lating the measured light intensity and the electrical conductivity of the solution  
182  $\sigma_{\text{w}}$  (in  $\text{S m}^{-1}$ ) (Fig. 2).

183 However, when using this calibration curve to infer local solution conduc-  
184 tivities inside the flow cell during subsequent tracer tests (which we present  
185 in section 4 below), we noticed that the largest conductivity values measured  
186 inside the cell were larger than the conductivity of the injected tracer solution.  
187 This unphysical result showed that the calibration curve obtained in the flow  
188 cell without solid grains (a standard Hele-Shaw cell), was not fully adequate for  
189 the tracer experiment cell. We have therefore assumed that a slight difference  
190 in the cell thickness, or perhaps the impact of the presence of the translucent  
191 solid grains, was responsible for the discrepancy. In particular, given the large  
192 fluorescein concentration in the injected tracer, it is not unreasonable to con-  
193 sider that some multiple scattering of the light emitted by the fluorescein may  
194 occur in the cell, with a fraction of the emitted light being absorbed by other  
195 fluorescein molecules on its way out from the cell, which is possible due to  
196 the overlapping emission and absorption spectra of fluorescein (see [45]). Ac-  
197 counting for this multiple scattering yields a prediction of the light intensity  
198 transmitted to the camera that is offset from the intensity measured in the ab-  
199 sence of multiple scattering by a factor which is a function of the flow cell's  
200 thickness. Hence a discrepancy in the cell thicknesses would lead to exactly this  
201 type of effect. Therefore, we have corrected the recorded calibration curve by  
202 assuming that the light intensity value calibrated in the pure Hele-Shaw cell for  
203 a given tracer concentration was offset by a given factor (independent of the

204 given tracer concentration) with respect to the correct value for the experimen-  
 205 tal cell. The correction factor of 0.805 has been inferred from the (reasonable)  
 206 constraint that the maximum conductivity value measured in the cell during the  
 207 experiment should exactly correspond to the conductivity of the injected tracer  
 208 solution. The corrected calibration curve is used systematically when inferring  
 209 local conductivities from light intensities in our experimental cell (Fig. 2).

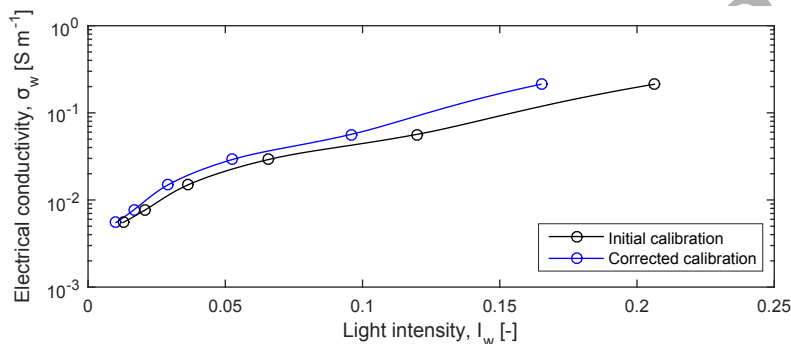


Figure 2: Initial and corrected calibration curves: pore water electrical conductivity  $\sigma_w$  as a function of the light intensity  $I_w$ .

## 210 2.2. Geoelectrical monitoring

211 The geoelectric monitoring is performed using a four electrode setup (see  
 212 Schlumberger [46] for the historical paper, and more recently Binley and Kemna  
 213 [7] for a more hydrology-oriented introductory text). We inject a current in the  
 214 two outer electrodes (C1 and C2) and measure the resulting electrical voltage  
 215 between the two inner electrodes (P1 and P2) (Fig. 1a). Given that the zone  
 216 of investigation is localized between P1 and P2, we chose not to have equally  
 217 spaced electrodes along the cell. The spacing between potential electrodes P1  
 218 and P2 is 97 mm in order to study the largest possible zone of the flow cell,  
 219 while the C1-P1 and P2-C2 spacings are 8 mm (Fig. 1).

220 The electrodes consist of a thin layer of copper (90  $\mu\text{m}$ ). They were inserted  
 221 at the bottom of the cylinder layer while manufacturing the cell; this ensured  
 222 good contact with the fluids in the cell without perturbing the flow. We chose

223 relatively wide electrodes, 2.5 mm for the current injection and 2 mm for the  
 224 potential measurement, to ensure a low contact resistance even at low water  
 225 saturation. The disadvantage of these large copper electrodes is that they block  
 226 the light between the light source and the camera, which results in a loss of  
 227 information about the fluid phases and concentration field located above them.

228 We measured the effective bulk electrical resistivity of the medium at a tem-  
 229 poral resolution of 2 s. We used a Campbell datalogger program for a half bridge  
 230 with four wires configuration (Fig. 1b). The datalogger imposes a 1 V electrical  
 231 potential difference between C1 and C2 that drives an electrical current in the  
 232 cell. The resulting electrical current and voltage between P1 and P2 is converted  
 233 into a bulk electrical resistance  $R^{\text{meas}}$  (in  $\Omega$ ). In order to obtain the effective  
 234 bulk electrical resistivity  $\rho^{\text{meas}}$  (in  $\Omega \text{ m}$ ), it is then necessary to determine the  
 235 geometrical factor of the cell,  $K_G$  (in m) such that  $\rho^{\text{meas}} = K_G R^{\text{meas}}$ . This  
 236 parameter was first estimated numerically in 3D using COMSOL Multiphysics  
 237 following the procedure described by Jougnot et al. [47] using the actual cell  
 238 geometry. The resulting estimate was  $K_G = 4.753 \times 10^{-4}$  m. For this setup,  
 239 the analytical solution for the 1D case (cell aperture area divided by the spacing  
 240 between the potential electrodes, see [7]) provides a close approximation to the  
 241 numerical model:  $K_G \approx 4.766 \times 10^{-4}$  m.

### 242 2.3. Electrical characterization of the porous medium and fluid phases geometry

243 Prior to the tracer tests, we first characterized the porous medium and the  
 244 geometry of the fluid phases from an electrical point of view, using a series of  
 245 electrical measurements with different homogeneous solute concentrations. To  
 246 do so, we first saturated the medium with one of the solutions obtained by di-  
 247 lution (i.e., with a given electrical conductivity  $\sigma_w$ ). Then, we jointly inject the  
 248 chosen solution (i.e., the wetting fluid) and the air (i.e., the non-wetting fluid)  
 249 to partly fill the medium with air while keeping the liquid phase connected  
 250 (thereby imposing partially saturated conditions). By varying the injection  
 251 rates of the fluids, we reached three or more steady state flows with different  
 252 saturations (i.e., proportion of wetting fluid in the porous space). By steady

253 state flows we refer to flows for which the spatial distributions of the fluid phases  
 254 change continuously, but their statistical properties (saturation, distribution of  
 255 cluster sizes, see [48]) are stationary. The steady state is considered to have  
 256 been reached when the saturation fluctuates around a plateau value, and the  
 257 longitudinal and transverse saturation profiles fluctuate around a uniform sta-  
 258 tionary profile. This can only be measured a posteriori, from the images. After  
 259 performing measurements with the largest saturation range ( $S_w$ ) possible with  
 260 the setup and experimental protocol (i.e.,  $S_w \in [0.46 ; 1]$ ), the procedure was  
 261 repeated with another concentration of the solution (i.e., another  $\sigma_w$ ). Note  
 262 that the lower saturation limit is linked to the connectivity of the liquid phase  
 263 and its stability overtime; liquid phase connectivity is necessary to allow mea-  
 264 surement of the bulk electrical conductivity. During these steps, both the bulk  
 265 electrical conductivity of the cell and the spatial distribution of the fluid phases  
 266 were recorded. These first series of measurements provided a set of images and  
 267 electrical conductivity measurements for different tracer solutions (i.e., different  
 268  $\sigma_w$ ) at different saturation degrees.

#### 269 2.4. Tracer test procedures

270 After these initial experiments, we conducted a tracer test under saturated  
 271 conditions and three tracer tests under partially saturated conditions.

272 For the fully saturated test, the medium was first saturated with the back-  
 273 ground solution ( $C_{\text{fluo}}^{\text{bkg}}$  and  $\sigma_w^{\text{bkg}}$ ) to obtain a homogeneous initial state. Then,  
 274 the tracer ( $C_{\text{fluo}}^{\text{tr}}$  and  $\sigma_w^{\text{tr}}$ ) was injected at a constant rate ( $1.375 \text{ mm}^3 \text{ s}^{-1}$ ). The  
 275 injection rate was chosen to be low enough to follow the dynamics with the sam-  
 276 pling frequency of our acquisition setup. It yields the dimensionless Reynolds  
 277 and Péclet numbers,  $\text{Re} = 1.64 \times 10^{-4}$  and  $\text{Pe} = 241$ , respectively. The test  
 278 was stopped when the measured electrical conductivity reached a constant value  
 279 (after  $\sim 12500$  s), that is, when an apparent steady-state was reached for the  
 280 salt concentration field.

281 For the tracer tests performed under partially-saturated conditions, an un-  
 282 saturated flow was first imposed by jointly injecting air and the background

283 solution at constant flow rates to reach a steady-state flow as explained in sec-  
 284 tion 2.3, with a given liquid saturation of the medium and a given size distribu-  
 285 tion of air clusters. After stopping the injection of air and background solution,  
 286 the tracer solution was injected continuously and at a volumetric flow rate that  
 287 was sufficiently low so that the impact on the previously-established air cluster  
 288 was minimal ( $0.277 \text{ mm}^3 \text{ s}^{-1}$ , yielding  $\text{Re} = 3.79 \times 10^{-4}$  and  $\text{Pe} = 68$ ). The  
 289 experiments were terminated when the measured bulk electrical conductivity of  
 290 the flow cell reached a constant value (after  $\sim 15200$  s for the test presented in  
 291 the results section).

### 292 3. Modelling approach

#### 293 3.1. From images to effective bulk electrical conductivity

294 The experiments described in the previous section provide two kinds of data:  
 295 images with a light intensity value per pixel,  $I(x, y)$ , on the one hand, and  
 296 an effective bulk electrical conductivity of the entire cell,  $\sigma^{\text{meas}}$ , on the other  
 297 hand. In this section, we describe how we simulate the effective bulk electrical  
 298 conductivity from the images in order to compare the computed conductivity,  
 299  $\sigma^{\text{sim}}$ , to the measured one,  $\sigma^{\text{meas}}$ .

300 The raw images are first corrected for spatial heterogeneities in the incident  
 301 light intensity (which is largest at the center of the flow cell). All subsequent  
 302 data processing is performed on these corrected images. Figure 3 shows the flow  
 303 chart used to process such a corrected image, and the subsequent electrical field  
 304 simulations. The flow cell geometry, with the exact geometry of the borders  
 305 and exact position of each cylinder, is obtained from an image of the medium  
 306 saturated with a solution at  $C_{\text{fluo}}^{\text{bkg}}$  and is stored as a binary image denoted “pore  
 307 space mask”, which defines the pore space:  $I_{\text{mask}} = 0$  for pixels positioned  
 308 inside borders and cylindrical grains, and 1 for pixels positioned within the  
 309 pore space. The electrodes are clearly visible in the images; their positions and  
 310 geometries are extracted and stored into another mask, the “electrode mask”.  
 311 The porosity of the medium is readily computed from the pore space mask:

312  $\phi = 0.73$ . Subsequent images ( $2966 \times 2308$  pixels) acquired during the course  
 313 of the experiments are used to extract (1) the phase distribution and (2) the map  
 314 of local conductivities at different times. Image pixels belonging to the air phase  
 315 are identified as those for which the mask value is 1 ( $I_{\text{mask}} = 1$ ) and the recorded  
 316 light intensity is null ( $I = 0$ ). The liquid (wetting fluid) phase is identified as  
 317 consisting of pixels for which  $I_{\text{mask}} = 1$  and  $I > 0$ ; we define a light intensity  
 318 map in the wetting phase,  $I_w(x, y)$ , equal to 0 outside the water phase, and  
 319 to  $I(x, y)$  inside the water phase. From this image processing, we can monitor  
 320 the water saturation during the tests by considering the ratio of the number of  
 321 pixels belonging to the water phase to the number of pixels belonging to the  
 322 entire pore space. Using the corrected calibration curve discussed in section 2.1  
 323 above, we then convert the  $I_w(x, y)$  map in to a map of local conductivities.

324 Using the spatial distributions of the phases and local tracer conductivities,  
 325 it is possible to simulate the cell's effective electrical bulk conductivity,  $\sigma^{\text{sim}}$ .  
 326 This numerical upscaling is based on the pixel distribution of electrical conduc-  
 327 tivity and is, therefore, limited by the image resolution. Using to the calibration  
 328 relationship between  $\sigma_w$  and the light intensity obtained from the different di-  
 329 lutions as described in paragraph 2.1, each pixel in the image is attributed a  
 330 given electrical conductivity  $\sigma_w(x, y)$  from  $I_w(x, y)$ . The electrical conductivity  
 331 of the wetting fluid ranges between  $\sigma_w = 0.0041$  and  $0.2130 \text{ S m}^{-1}$ . In the  
 332 simulations, the electrodes were given an electrical conductivity of  $\sigma_{\text{elec}} = 10^4$   
 333  $\text{S m}^{-1}$ , which is sufficiently high to obtain practically-constant isopotential val-  
 334 ues along the electrodes but also small enough to avoid numerical problems. The  
 335 polymer NOA81 (cylinders and borders) is, similarly to the air phase, a non-  
 336 conducting material and an arbitrary low electrical conductivity is assigned to  
 337 both:  $\sigma_{\text{NOA81}} = \sigma_{\text{air}} = 10^{-6} \text{ S m}^{-1}$ , which is a value sufficiently low to avoid  
 338 significant electrical current flow in these materials while allowing convergence  
 339 of the numerical code. These electrical simulations will help understand ex-  
 340 actly where the electrical current is flowing and its links with solute transport  
 341 processes.

342 The numerical upscaling of the electrical conductivity consists in solving

343 the Poisson equation in 2D. We use a modified version of the code MaFlot  
 344 (www.maflot.com) initially designed to address density-driven Darcy flows [49].  
 345 In the simulations, we generate the current flow by imposing an electrical voltage  
 346 of 1 V between the current electrode (C1 and C2) (see Fig. 1). The top and bot-  
 347 tom boundary conditions are set to electrical insulation. The electrical problem  
 348 is therefore a boundary problem that can be seen as an analog to determining  
 349 the effective hydraulic conductivity of a porous medium of heterogeneous perme-  
 350 ability field between two reservoirs with a given pressure difference under steady  
 351 state conditions. Note that imposing a potential difference in the modelling in-  
 352 stead of injecting a fixed electrical current presents two main advantages: (1) it  
 353 corresponds to what is done experimentally and (2) it avoids problems related  
 354 to air clusters on the electrodes. Indeed, injecting a fixed current would require  
 355 a perfect knowledge of the wetting phase and solute concentration above the  
 356 electrode, which is impossible with the present experimental setup.

### 357 3.2. Petrophysical characterization

358 Many petrophysical relationships have been proposed to relate electrical con-  
 359 ductivity to porosity, water saturation, and electrolyte concentration (e.g., [6]).  
 360 The experiments described in section 2.3 provided various data sets of measured  
 361 electrical conductivities  $\sigma^{\text{meas}}$  for different water saturations  $S_w$  at three differ-  
 362 ent saline tracer conductivities  $\sigma_w$ . Figures 4a and b show  $\sigma^{\text{meas}}$  for different  
 363  $\sigma_w$  under saturated and partially saturated conditions, respectively.

364 Among the existing petrophysical relationships, let us consider the model  
 365 that is the most used in the ERT literature: the classical model that is obtained  
 366 by combining the so-called Archie's first and second law [50]. It is applica-  
 367 ble when the mineral surface conductivity can be neglected (i.e., typically for  
 368 materials with low specific surface area such as sands or sandstones):

$$\sigma = \frac{S_w^n}{F} \sigma_w, \quad (1)$$

369 where  $\sigma$  and  $\sigma_w$  are the electrical conductivities ( $\text{S m}^{-1}$ ) of the porous medium  
 370 and pore-water, respectively,  $S_w$  is the water saturation (-),  $F$  is the electri-

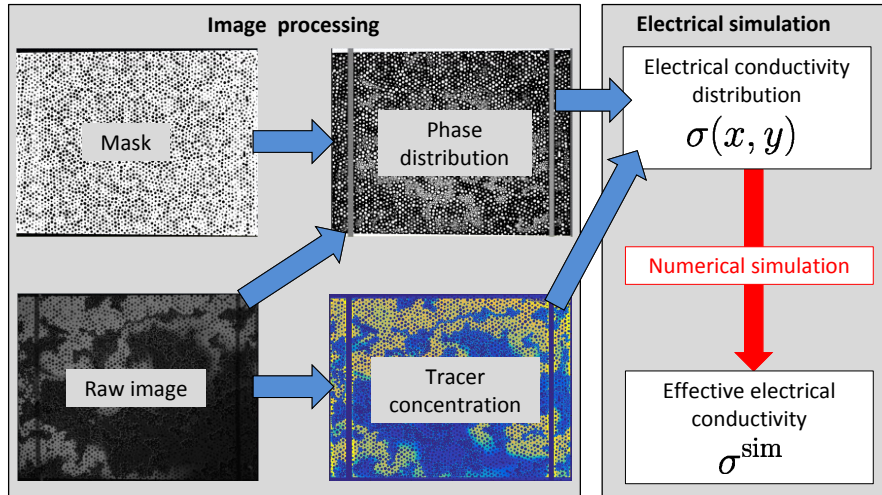


Figure 3: Schematic representation of the processing of the light-corrected images and the corresponding numerical simulation.

cal formation factor (-), and  $n$  is the saturation exponent (-). The electrical  
 formation factor is related to porosity by a power law:  $F = \phi^{-m}$  where  $m$  is  
 the so-called cementation exponent. The parameters  $m$  and  $n$  depend on the  
 pore-space and water phase geometry, respectively [e.g., Friedman 51]. The  
 petrophysical parameters obtained by optimization, using the Simplex algo-  
 rithm (Caceci and Cacheris [52]) and considering the entire dataset, are  $F =$   
 1.85 and  $n = 4$ .

Equation (1) relating  $\sigma$  and  $\sigma_w$  allows us to reproduce very well the exper-  
 imental data in saturated conditions (Fig. 4a), but the data fit is not as good  
 for partially-saturated conditions (Fig. 4b). One likely reason for this is that  
 the sample size is too small to produce a representative elementary volume for  
 the experiments with the lowest water saturations.

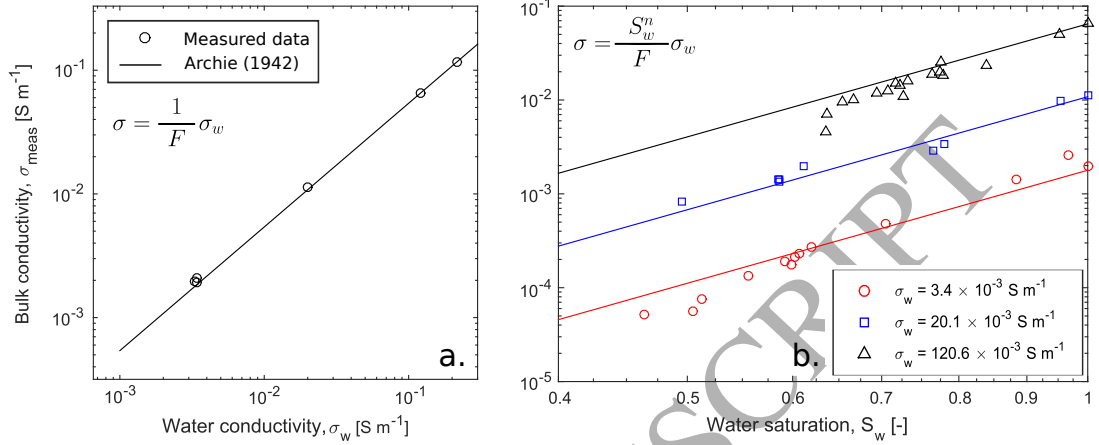


Figure 4: Bulk electrical conductivity as a function of (a) water conductivity in saturated conditions and (b) water saturation for different pore-water electrical conductivities. The dots (circles, squares, and triangles) correspond to the measurements (for different solutions) and the plain lines corresponds to the model of Archie [50]. The best fit to the entire data set was achieved with  $F = 1.85$  and  $n = 4$  in Eq. 1.

Eq. (1) is based on the assumption that the pore water salinity is homogeneously distributed in the wetting phase. In the literature, ERT monitoring results of saline tracer tests are often interpreted by reformulating Eq. 1 and assuming that the water saturation is known. This results in an ERT-inferred electrical conductivity of the solute at the resolution scale:

$$\sigma_w^{\text{app}} = \frac{F}{S_w^n} \sigma^{\text{meas}}. \quad (2)$$

This apparent solute electrical conductivity can then be used to estimate an average solute concentration in the considered volume. For a spatially-constant  $F$ ,  $S_w$  and  $n$ ,  $\sigma_w^{\text{app}}$  is theoretically limited by the Wiener bounds ([53]), sometimes called Voigt and Reuss bounds.

The Wiener bounds are the arithmetic,  $\bar{\sigma}_w^a$ , and harmonic,  $\bar{\sigma}_w^h$ , means of the electrical conductivities  $\sigma_i$  constituting the wetting phase:

$$\bar{\sigma}_w^a = \frac{1}{N} \sum_{i=1}^N \sigma_w^i, \quad (3)$$

$$\bar{\sigma}_w^h = \frac{N}{\sum_{i=1}^N \frac{1}{\sigma_w^i}}, \quad (4)$$

where  $i$  denotes a single pixel belonging to the wetting phase and  $N$  is the total number of pixels identified as the wetting phase. The arithmetic and harmonic means are equivalent to the global conductivity of an electrical circuit where conductances would be placed either in parallel or in series, respectively. The Wiener bounds theory predicts that:

$$\bar{\sigma}_w^a \geq \sigma_w^{\text{app}} \geq \bar{\sigma}_w^h. \quad (5)$$

## 392 4. Results

393 This section describes and analyzes the data obtained from the laboratory  
394 tracer experiments (section 2) after data-processing following the workflow de-  
395 picted in section 3.1. We first present the results from the tracer test in saturated  
396 conditions and then those obtained under partially-saturated conditions.

### 397 4.1. Tracer test under saturated conditions

398 Figure 5a shows the evolution of the measured bulk electrical conductivity  
399 during the tracer test performed in the water-saturated flow cell;  $t = 0$  s corre-  
400 sponds to the beginning of the tracer injection in the cell. Figures 5b to e are  
401 snapshot images of the normalized tracer concentration at  $t = 4000$  s, 6000 s,  
402 8000 s, and 12000 s, respectively.

403 As expected, the measured bulk electrical conductivity increases as the tracer  
404 invades the medium. This increase is relatively smooth as a consequence of  
405 the tracer being transported according to an advection-diffusion process in a  
406 medium that is homogeneous at the Darcy scale. The tracer front is not per-  
407 fectly straight nor transverse to the mean flow direction, due to some transverse  
408 heterogeneity in the conditions of tracer injection at the inlet of the medium,  
409 and possibly to a slight transverse permeability gradient in the medium. But no  
410 solute fingers are visible at scales smaller than a third of the flow cell width, and

411 when the most advanced solute finger reaches the medium outlet, the most re-  
 412 tarded region of the front has already reached half of the medium's length. Note  
 413 that the rate of increase in the bulk electrical conductivity accelerates between  
 414  $t = 4000$  and  $8000$  s (Fig. 5a), which corresponds to the time interval over which  
 415 increasing tracer concentration is in contact with both potential electrodes (P1  
 416 and P2). The rate of increase decreases after  $t = 8000$  s when a continuous strip  
 417 of highly concentrated tracer joins the two electrodes. This enables electrical  
 418 current to flow through the cell with a lesser resistance.

419 After post-processing the images and solving the electrical problem at each  
 420 time step (see section 3.1), it is possible to compare the measured bulk con-  
 421 ductivity (i.e., flow cell scale, or macroscopic scale) to the simulated ones. Fig-  
 422 ure 6a shows that the simulated conductivity ( $\sigma^{\text{sim}}$ ) is in relatively good agree-  
 423 ment with the data ( $\sigma^{\text{meas}}$ ) measured at the cell scale (root mean square error:  
 424  $RMSE = 0.0021 \text{ S m}^{-1}$ ).

425 Figure 6b shows the evolution of the apparent electrical conductivity of the  
 426 wetting phase  $\sigma_w^{\text{app}}$  at the macroscopic scale (i.e., the scale of the flow cell)  
 427 using Eq. 2. This value is compared to the arithmetic mean (“conductance  
 428 in parallel” model)  $\bar{\sigma}_w^{\text{a}}$  and to the harmonic mean (“conductance in series”  
 429 model)  $\bar{\sigma}_w^{\text{h}}$ , showing that Eq. 5 is respected. Initially,  $\sigma_w^{\text{app}}$  tends to follow the  
 430 conductance in series model ( $\bar{\sigma}_w^{\text{h}}$ ) until fluid carrying a significant concentration  
 431 of the tracer reaches the second potential electrode P2 (between  $t = 3000$  s  
 432 and  $t = 9000$  s). Then,  $\sigma_w^{\text{app}}$  starts to follow the conductance in parallel model  
 433 ( $\bar{\sigma}_w^{\text{a}}$ ) as the tracer tends to be distributed more homogeneously in the pore  
 434 space. Note that at the end of the tracer test, the pore space is not filled  
 435 homogeneously by the tracer ( $\bar{\sigma}_w^{\text{a}} \neq \bar{\sigma}_w^{\text{h}}$ ). Even with this homogeneous grain  
 436 distribution, some parts of the medium are left with comparatively low tracer  
 437 concentrations (Fig. 5e).

#### 438 4.2. Tracer test under partially-saturated conditions

439 The same procedure was applied to the data obtained from the two-phase  
 440 flow tracer test. Figure 7a shows the evolution of the measured electrical con-

ductivity during the tracer test, while Figs. 7b, c, and d are snapshot images of the normalized tracer concentration at times  $t = 2000$  s, 4000 s, 8000 s, and 14000 s after the beginning of the tracer injection in the cell, respectively. The non-wetting phase (air) appears in white, while the grains, boundaries, and electrodes appear in black. The air phase is arranged in clusters with a geometry that changed during the course of the experiment (i.e., a saturation increase from  $S_w = 0.69$  to 0.87). Note that the strategy described in Section 3.1 allows us to account for these saturation changes in the simulations.

As for the saturated case, Figure 7a shows a strong increase in the bulk electrical conductivity as the tracer invades the medium. However, this increase is sharper and it appears earlier than for the saturated case. In partially saturated conditions, the tracer has a much reduced freedom to choose its pathway through the medium as not only grains act as obstacles to flow (as in the saturated case), but also large air clusters (e.g., [35]). The path for the tracer includes more obstacles (grains + air clusters), having a higher mean interstitial velocity. This results in a larger heterogeneity of the tracer concentration in the flow cell.

In agreement with the experiment under saturated conditions (see Section 4.1), a sharp increase in the effective bulk electrical conductivity occurs when the tracer connects the P1 and P2 electrodes, creating a preferential pathway of least resistance for the electrical current (around  $t = 4000$  s). One can also identify a second smaller increase around  $t = 9000$  s when other fingers of tracer reach the P2 electrodes, thereby, creating new preferential pathways for the electrical current. The initial small fingering feature occurring at the top of the cell (Fig. 7c) generates a larger relative increase in  $\sigma^{\text{meas}}$  (from  $10^{-3}$  to  $10^{-2}$  S m $^{-1}$  between  $t = 2000$  s and  $t = 6000$  s) than the larger fingers of tracer that can be seen in Fig. 7d (from  $10^{-2}$  to  $2 \times 10^{-2}$  S m $^{-1}$ ). Fingering thus leads to strong increases in the electrical conductivity.

Figure 8a shows the comparison between the measured and the simulated electrical conductivities at the scale of the flow cell. The match between the simulation and the measurements, obtained with the same calibration curve

472 as for the saturated experiment, is relatively good except at the beginning  
 473 ( $RMSE = 0.0017 \text{ S m}^{-1}$ ). The small discrepancy could be explained by the  
 474 fact that the optical contrast between the background solution and the air is  
 475 somewhat too low in comparison to the intensity range corresponding to the  
 476 heterogeneity of the lighting setup, so that even after correcting the images for  
 477 lightning heterogeneity a small number of the air clusters are not detected as  
 478 such, but are attributed to the background solution. The apparent electrical  
 479 conductivity of the wetting phase at the macroscopic scale (i.e., the medium's  
 480 scale or flow cell scale),  $\sigma_w^{\text{app}}$ , was calculated using Eq. 2 and considering the  
 481 water saturation obtained from the image processing (Fig. 8a) and the best fit  
 482 parameters from the petrophysical characterization ( $F = 1.85$  and  $n = 4$ , see  
 483 Fig. 4). Note that the data respect Eq. 5 during most of the tracer test dura-  
 484 tion, except at for some points at the beginning of the test.  $\sigma_w^{\text{app}} > \bar{\sigma}_w^{\text{a}}$  (before  
 485  $t = 1500 \text{ s}$ ) and  $\sigma_w^{\text{app}} < \bar{\sigma}_w^{\text{h}}$  (for  $t = 2500$  and  $3000 \text{ s}$ ) can be explained by the  
 486 poor fit between the measured and simulated electrical conductivities at the  
 487 corresponding times. Similarly to the saturated case,  $\sigma_w^{\text{app}}$  first tends to follow  
 488 the “conductance in series” model before the first tracer finger connects P1 and  
 489 P2 (Fig. 7c). Then,  $\sigma_w^{\text{app}}$  tends towards the “conductance in parallel” model  
 490 but never reaches its values. Indeed, throughout the tracer test, the medium  
 491 never reaches a homogenized distribution of tracer concentration over the time  
 492 of the experiment. Figure 7e clearly shows the very heterogeneous nature of the  
 493 tracer distribution after  $t = 14000 \text{ s}$ , which explains why  $\bar{\sigma}_w^{\text{h}}$  does not converge  
 494 to  $\bar{\sigma}_w^{\text{a}}$ . The homogenization might occur after a much longer time through  
 495 diffusion processes along the concentration gradients. Ionic diffusion processes  
 496 have very slow kinetics (of order  $D = 10^{-10} \text{ m}^2 \text{ s}^{-1}$ ) compared to the advec-  
 497 tion processes studied here: taking the linear size of the largest air clusters,  
 498  $l_{\text{air}} \simeq L/4 = 40 \text{ mm}$  as a typical length scale, the time necessary for the con-  
 499 centration to fully homogenize by ionic diffusion would be  $l_{\text{air}}^2/D = 1.6 \times 10^7 \text{ s}$   
 500  $= 185 \text{ days}$ .

501 **5. Discussion**

502 *5.1. Petrophysical characterization of the 2D medium*

503 The petrophysical characterization of the analogous 2D porous medium is  
 504 an important step for the interpretation of the present experiments.  $F = 1.85$   
 505 and  $n = 4$  can seem surprising for petrophysicists used to natural rocks. The  
 506 low value of the formation factor is a consequence of the large porosity, and the  
 507 high value of the exponent  $n$  is the consequence of the 2D nature of the media  
 508 under investigation (see the 2D pore network study of Mainault et al. [54]).  
 509 Based on Archie [50], the electrical tortuosity of the wetting phase,  $\alpha_w$ , can be  
 510 defined as (Revil and Jougnot [55]):

$$\alpha_w = \phi F S_w^{(1-n)}, \quad (6)$$

511 which yields  $\alpha_w = 1.35$  and  $\alpha_w = 4.04$  at the beginning of the saturated and  
 512 partially saturated tracer tests, respectively. These small tortuosities can be  
 513 visualized by considering the phase distributions (e.g., only 2D obstacles, long  
 514 continuous path of wetting phase, see Figs. 5 and 7). Note that the electrical tor-  
 515 tuosity of the water phase determined by electrical conductivity measurements  
 516 can be used to predict different transport properties of interest in hydrology,  
 517 such as the ionic and gas diffusion coefficients (e.g., [55, 56, 57]) or thermal  
 518 conductivity (e.g., [58, 59]).

519 Figure 4 shows that the fit of Archie's model for data obtained at full sat-  
 520 uration is better than the fit obtained under partially saturated conditions.  
 521 This can be explained by considering the concept of Representative Elementary  
 522 Volume (REV): the smallest volume over which a measurement can be made  
 523 to obtain a value representative of the whole ([60]). For saturated conditions  
 524 with a homogeneous solution concentration (Fig. 4a), we conducted numerical  
 525 tests by calculating the bulk conductivity  $\sigma^{\text{calc}}$  of only parts of the cell (not  
 526 shown here). These tests showed that the difference between the bulk electrical  
 527 conductivity calculated over a quarter of the cell and over the entire domain  
 528 was smaller than 1.26 %. Thus demonstrating that the REV of the saturated

529 medium  $REV^{\text{sat}}$  is smaller than the flow cell. However, substantial differences  
 530 between sub-domains occurred when we conducted a similar numerical study  
 531 on the partially saturated medium. Therefore, the size of REV for the partially  
 532 saturated medium,  $REV^{\text{unsat}}$  is likely larger than the size of the cell itself. This  
 533 is expected as the linear size of the largest air clusters in the medium is of  
 534 about half of the medium size. Consequently, we illustrate here the following  
 535 inequality:

$$REV^{\text{sat}} \ll REV^{\text{unsat}}. \quad (7)$$

536 This is well-known in the literature (e.g., [61]), but it is not always accounted  
 537 for in hydrogeophysical studies. The limitations of Archie's law in the presence  
 538 of percolation phenomena are discussed, for instance, by Kozlov et al. [43].

### 539 *5.2. Relationship between the concentration field and the measured conductivity*

540 As shown in section 4, the heterogeneity of the tracer concentration field  
 541 strongly depends on the saturation of the medium. Indeed, the concentration  
 542 field is much more heterogeneous under partially saturated conditions than in  
 543 the saturated case. As seen in Fig. 7d, at the end of the experiment ( $t = 14000$  s),  
 544 large parts of the cell are still at the background solution concentration and the  
 545 tracer is far from being homogeneously distributed. Note that molecular/ionic  
 546 diffusion effects will eventually homogenize the tracer concentration but with  
 547 very slow kinetics (see discussion in [35]).

548 Figure 9 compares the normalized tracer concentration distribution at a late  
 549 stage of saturated and partially-saturated tracer tests and the corresponding  
 550 simulated electrical current densities. The impact of the saturation distribution  
 551 has a strong effect on the tracer distribution (Figs. 9a and b) that clearly man-  
 552 ifest itself in simulated electrical current densities in saturated (Fig. 9c) and  
 553 partially-saturated (Fig. 9d) conditions. In the fully saturated media, we find a  
 554 current density that is homogeneously-distributed in the pore space, while in the  
 555 partially-saturated case it is highly channelized. We find that the current paths  
 556 are straighter and less tortuous than the saline tracer distribution (Figs. 9c and

557 d). As expected, while the saturated porous media shows a homogeneous dis-  
558 tribution of current densities, the unsaturated porous media is characterized by  
559 a highly channelized current density field.

560 In our experimental results, we show that the effective bulk electrical conduc-  
561 tivity at the scale of the flow cell carries information about transport processes  
562 occurring at smaller scales. Electrical conductivity is sensitive to the saline  
563 tracer distribution in the medium. Indeed, for both saturated and partially-  
564 saturated conditions, a very strong increase of the effective bulk electrical con-  
565 ductivity can be seen when the saline tracer connects electrodes P1 and P2  
566 (Figs. 5 and 7). The connectivity of the tracer in the medium is illustrated by  
567 the Wiener bounds; the apparent water conductivity is initially analogous to a  
568 model of conductance in series before it starts to follow a model of conductances  
569 in parallel. This analysis is even more instructive in partially saturated condi-  
570 tions as the breakthrough of only one solute finger through the medium acts as  
571 a preferential path for the electrical current, yielding a very strong change in  
572 bulk electrical conductivity.

573 Tracer fingers in the unsaturated case act as preferential paths for the electri-  
574 cal current (Fig. 9d) in comparison to the more homogeneous case in saturated  
575 conditions (Fig. 9b). One can identify “bottle-necks” as the places where the  
576 flow lines are focused between air clusters or grains (e.g., [35]). This effect on the  
577 tracer transport affect the distribution of the electrical current flow (Fig. 9d).  
578 This channeling of the electrical current density is not only controlled by the  
579 tracer concentration alone, but also by how a region containing high tracer  
580 concentrations connects the different electrodes of the measurement setup. For  
581 example, the large tracer concentration area in the middle of Fig. 9d does not  
582 contribute significantly to the electrical flow.

583 The dynamics and evolution of the effective tracer percolation through the  
584 medium are also well captured by the bulk electrical conductivity. In saturated  
585 conditions, the smooth increase of  $\sigma$  during the entire tracer test corresponds  
586 to the progressive invasion of the flow cell by the saline tracer (Fig. 5). On  
587 the contrary, the more abrupt increase of  $\sigma$  around  $t = 4000$  s and the smaller

588 one around  $t = 9000$  s (Fig. 7) denote the percolation of the first and second  
 589 fingers of tracer through the porous medium. This clear link between tracer  
 590 percolation and bulk electrical conductivity should be studied in more details to  
 591 couple transport models at the pore-scale and hydrogeophysical measurements,  
 592 for example following the idea proposed by Kemna et al. [9] at the field-scale.

### 593 5.3. Electrical conductivity anisotropy

594 From the previous subsection, it appears that the bulk electrical conductivity  
 595 is strongly related to the liquid phase connectivity and to the spatial distribution  
 596 of the tracer concentration. It is therefore highly sensitive to the orientation of  
 597 the electrical conductivity measurement setup with respect to the tracer trans-  
 598 port. In order to study this effect, numerical tests have been performed: for  
 599 each time step, the simulated bulk electrical conductivity presented in sections  
 600 4.1 and 4.2 (the longitudinal bulk electrical conductivity) has been compared to  
 601 the value obtained from a numerical simulation where the current flows in the  
 602 medium from top to bottom, so that we compute the transverse bulk electrical  
 603 conductivity. That is, we extracted the section of the images between electrode  
 604 P1 and P2 (i.e., the investigation zone) and solved the electrical problem after  
 605 imposing a  $90^\circ$  rotation to the porous medium around its center, without mod-  
 606 ifying the position of the electrodes. Figures 10a and b illustrate the simulation  
 607 set-up of this anisotropy study, while Fig. 10c and d show the anisotropy factor  
 608  $\lambda$  of the electrical conductivity during the saturated and the partially saturated  
 609 tracer tests, respectively. The dimensionless anisotropy factor,  $\lambda$ , is calculated  
 610 as follows [e.g. 62]:

$$\lambda = \sqrt{\frac{\sigma^{\text{sim}}}{\sigma_{90}^{\text{sim}}}}, \quad (8)$$

611 where  $\sigma^{\text{sim}}$  and  $\sigma_{90}^{\text{sim}}$  are the longitudinal and the transverse electrical conduc-  
 612 tivities with respect to the fluid flow direction, respectively. Finally, Figures 10e  
 613 and f are conceptual illustrations of ERT measurements for a lateral or vertical  
 614 tracer test in the near surface, respectively.

615 The behaviour of the electrical anisotropy factor is completely different under  
 616 saturated and partially saturated conditions (Fig. 10). Under saturated condi-  
 617 tions (Fig. 10b), the bulk electrical conductivity of the medium is isotropic (i.e.,  
 618  $\lambda \simeq 1$ ) at the beginning and at the end of the tracer test. During the tracer  
 619 test, the transverse electrical conductivity is higher than the longitudinal one  
 620 as the zone that is invaded by the tracer create a high conductivity path for the  
 621 electrical current from top to bottom (Fig. 5). On the contrary, under partially  
 622 saturated, the medium is already anisotropic due to the presence of air clusters,  
 623 the largest of which have a linear size close to half the medium size. Given the  
 624 flow direction in the cell, air clusters tend to be more elongated in the longitu-  
 625 dinal direction (Fig. 7), which yield  $\sigma^{\text{sim}} > \sigma_{90}^{\text{sim}}$  ( $\lambda = 1.15$  for  $t = 0$  s). Then, as  
 626 the tracer propagates in the pore space, the complex patterns of tracer fingering  
 627 tend to increase the anisotropy factor (up to  $\lambda = 2.41$ ). Note that, at the end  
 628 of the tracer test, the anisotropy factor diminishes but does not return to its  
 629 initial value (e.g.  $\lambda = 1.59$  at  $t = 14000$  s). This is caused by the remaining  
 630 strong heterogeneity in the tracer concentration distribution (Fig. 9).

#### 631 5.4. Impact on ERT interpretations

632 This study presents a new geoelectrical milli-fluidic setup that helps un-  
 633 derstanding better the link between state variables of hydrogeological interest  
 634 (water saturation, flow velocity field, ionic concentration field, solute concen-  
 635 tration field) and measurable upscaled geophysical properties under dynamic  
 636 conditions. Considering that the scale of the flow cell in our experiment could  
 637 be seen as an analogue to the resolution scale in a field ERT experiment, the  
 638 present work has clearly shown that the apparent water electrical conductiv-  
 639 ity at the resolution scale is largely determined by the heterogeneity of ionic  
 640 concentrations below this resolution scale, especially under partially saturated  
 641 conditions (see Figs. 5 to 9).

642 Electrical conductivities resulting from ERT inversion are subjected to two  
 643 kinds of processes masking the medium heterogeneity: (1) a smoothing above  
 644 the cell size used to discretize the subsurface that is due to the inversion reg-

ularization imposed to make the inverse problem unique and (2) the conductivity homogenization at the REV (or discretized cell size) scale that we study herein. The inversion smoothing is the most scrutinized one as it is due to a regularization process needed to perform the inversion [e.g. Constable et al. 22]. Various works have described and studied the impact of model regularization, showing that information about sharp contrasts between model cells is lost (see, among other works: Day-Lewis et al. [18], Singha and Gorelick [19]). This phenomenon induces an apparent tracer loss when conducting in situ ERT monitoring of tracer tests. The second process masking the heterogeneity of the processes at play is a consequence of unaccounted saline tracer heterogeneity below the cell size used in the inversion. This cell size is often implicitly assumed to correspond to the REV scale and petrophysical models are used (see Eq. 1) that assumes that saline tracer heterogeneity is constant. Only a few works have considered tracer heterogeneity at the REV scale (e.g., [23], [28]), but only for two classes of porosities. Future work is needed to ensure proper upscaling to the cell size used in geophysical inversion and forward modeling. This work has clearly demonstrated that such effects can be very strong. In practice, we suggest that both of these effects are interconnected and we refer to them collectively as sub-resolution effects.

In our experiments we find that the heterogeneous fluid phase distributions and ionic concentration field in the aqueous phase at the sub-resolution scale have shown a strong impact on the effective bulk electrical conductivity. When conducting ERT monitoring, researchers often try to retrieve the ionic concentration at the resolution scale from the bulk electrical conductivity using a petrophysical relationship (often Archie [50], Eqs. 1 and 2) which assume a homogeneous distribution of  $\sigma_w$  below the resolution scale. Thus, they ignore the two effects described above (regularization and homogenization). However, in section 4, we have shown that the bulk electrical conductivity measured at the scale of our porous medium depends strongly on the connectivity of the tracer between the two potential electrodes at the pore-scale. Figures 6b and 8b show that as long as the medium is not homogeneous, the apparent water

676 conductivity can be much smaller than the arithmetic mean of its constituents:  
 677  $\sigma_w^{\text{app}} \ll \bar{\sigma}_w^{\text{a}}$ . Indeed, the electrical current is only sensitive to a fraction of the  
 678 tracer in the medium, the part connecting both sides of the voxel in the direc-  
 679 tion of the electrical current, as shown by Fig. 9. And, as discussed previously,  
 680 the time of homogeneization can be much longer than the duration of an ex-  
 681 periment (be it a lab or a field experiment). This inequality between effective  
 682 bulk conductivity and arithmetic average conductivity results in an apparent  
 683 mass loss when inferring solute concentrations from ERT inversion results using  
 684 Eq. (2). Indeed, in our medium, the arithmetic mean of the local conductivities  
 685 (the upper Wiener bound),  $\bar{\sigma}_w^{\text{a}}$ , is proportional to the arithmetic mean of local  
 686 concentrations, which is the solute concentration defined at the medium scale.  
 687 If one considers that our medium scale represents the resolution scale of an  
 688 ERT field experiment (Figs. 10e and f), the solute concentration measured by  
 689 ERT would be inferred from an apparent water conductivity measured at that  
 690 scale, and hence its ratio to the true solute concentration would equal the ratio  
 691  $\sigma_w^{\text{app}}/\bar{\sigma}_w^{\text{a}}$ . In other words the apparent mass loss is a necessary consequence of  
 692 the upper Wiener bound at sub-resolution scale and is to be expected as soon as  
 693 the solute is not well-mixed in the pore space and at the ERT resolution scale  
 694 (i.e., always). This mechanism could account for an important proportion of the  
 695 very important mass loss in ERT studies (e.g., 75 % of apparent mass loss in  
 696 Singha and Gorelick [10]). Furthermore, these results indicate that monitoring  
 697 an horizontal tracer flow (Fig. 10e) or a vertical one (Fig. 10f) from the surface  
 698 could result in very different apparent mass losses, depending also on the type  
 699 of ERT measurements performed (surface measurements or borehole measure-  
 700 ments). The use of electrode arrays at both the surface and in boreholes [e.g.  
 701 14], when available, could help better constraining the tracer flow direction by  
 702 taking advantage of this anisotropy.

703 Finally, to the best of our knowledge, the electrical conductivity has never  
 704 been considered a tensor in time-lapse ERT inversions [see 63, 64, for static in-  
 705 version]. Therefore, the effect of tracer percolation on the electrical conductivity  
 706 anisotropy factor is largely ignored and will inevitably produce artifacts. Given

707 the large value obtained in the anisotropy test (up to  $\lambda = 2.76$  in Fig. 10d),  
708 it seems that describing electrical conductivity as a tensorial property during  
709 tracer tests should be investigated in more details.

#### 710 *5.5. Technical improvements for further experiments*

711 We have developed a geoelectrical milli-fluidic setup to study sub-resolution  
712 effects associated with electrical conductivity monitoring of tracer tests. Even  
713 if this initial study is already rich in results, significant improvements could be  
714 made to the experimental setup and measurement protocol.

715 The opacity of the currently used electrodes has the disadvantage of de-  
716 grading the information available about what is happening above them (Figs.  
717 5, 7, and 9), making for example the determination of air cluster boundaries  
718 above an electrode difficult. Different possibilities can be explored to solve this  
719 issue, among which the use of transparent electrodes, or locating the electrodes  
720 outside of the porous medium.

721 An appropriate choice of fluorescein concentration in the injected solutions  
722 is crucial to obtain high-quality images with a suitable optical contrast. For  
723 future works, we recommend that the background solution should be more con-  
724 centrated in fluorescein, in order to improve the contrast between the liquid  
725 phase at low fluorescein concentration and the air phase. Furthermore, the  
726 mass concentration ratio between fluorescein and NaCl salt should be revisited  
727 to take advantage of the largest range of light intensity possible. We anticipate  
728 that performing the calibration of the transfer function between light intensity  
729 and local conductivity in the same flow cell as that used for the tracer exper-  
730 iments will remove the need for an a posteriori correction of the calibration  
731 curve. Besides, the use of many more calibration points will help improving the  
732 reliability of that curve.

## 733 **6. Conclusion**

734 We propose a new geoelectrical milli-fluidic setup to study the impact of the  
735 pore-scale distribution of fluid phases and tracer concentrations on the effective

736 bulk electrical conductivity. The setup is based on a two-dimensional porous  
737 medium consisting of a single layer of cylindrical grains positioned randomly be-  
738 tween two parallel glass plates. The macroscopic scale in our laboratory study  
739 can be seen as an analogue to the resolution scale of ERT at the field-scale.  
740 After performing a petrophysical characterization of the porous medium, we  
741 monitored variations in the bulk electrical conductivity of the porous medium  
742 during saline tracer tests under full and partial saturation. We find that the  
743 air distribution and the resulting heterogeneity in solute concentrations lead to  
744 electrical current channeling with strong effects on effective bulk conductivities.  
745 This suggests a strong impact of pore-scale and sub-resolution effects on up-  
746 scaled bulk electrical conductivity in terms of magnitude and anisotropy. Such  
747 effects are expected to systematically occur at the field-scale due to incomplete  
748 solute mixing below the resolution scale. We suggest that they could contribute  
749 significantly to an important inconsistency in conventional time-lapse ERT im-  
750 age processing, namely the apparent loss of tracer mass. In fact, the use of  
751 the upper Wiener bound of the effective bulk electrical conductivity implies  
752 that the inferred solute concentration at the ERT resolution scale will always  
753 be smaller than the true average solute concentration at that scale. The pre-  
754 sented geoelectrical milli-fluidic setup (and variations thereof) opens up a range  
755 of opportunities to investigate the link between electrical signals and a variety  
756 of pore-scale processes, such as mixing, reactive transport, and biogeochemical  
757 reactions.

#### 758 **Acknowledgment**

759 The authors gratefully acknowledge support from the EC2CO program of  
760 INSU/CNRS (project AO2014-906387). The experimental work was also sup-  
761 ported by the Interreg project CLIMAWAT, EU-RDF INTERREG IVA France  
762 (Channel)-England program. The data used are available by contacting the  
763 corresponding author. The authors gratefully thank the editor, Kamini Singha,  
764 and an anonymous reviewer for their very constructive comments.

765 **References**766 **References**

- 767 [1] S. S. Hubbard, Y. Rubin, Introduction to hydrogeophysics, in: Hydrogeo-  
768 physics, Springer, 2005, pp. 3–21.
- 769 [2] R. Guérin, Borehole and surface-based hydrogeophysics, *Hydrogeology*  
770 *Journal* 13 (1) (2005) 251–254.
- 771 [3] A. Binley, G. Cassiani, A. Revil, K. Titov, H. Vereecken, *Applied Hydro-*  
772 *geophysics*, Springer, 2006.
- 773 [4] S. Hubbard, N. Linde, Hydrogeophysics, in: P. Wilderer (Ed.), *Treatise on*  
774 *Water Science*, Vol. 1, Oxford: Academic Press, 2011, pp. 401–434.
- 775 [5] A. Binley, S. S. Hubbard, J. A. Huisman, A. Revil, D. A. Robinson,  
776 K. Singha, L. D. Slater, The emergence of hydrogeophysics for improved un-  
777 derstanding of subsurface processes over multiple scales, *Water Resources*  
778 *Research* 51 (6) (2015) 3837–3866.
- 779 [6] P. Glover, Geophysical properties of the near surface earth: electrical prop-  
780 erties, *Treatise on Geophysics* 11 (2015) 89–137.
- 781 [7] A. Binley, A. Kemna, Dc resistivity and induced polarization methods, in:  
782 *Hydrogeophysics*, Springer, 2005, pp. 129–156.
- 783 [8] A. Revil, M. Karaoulis, T. Johnson, A. Kemna, Review: Some low-  
784 frequency electrical methods for subsurface characterization and monitor-  
785 ing in hydrogeology, *Hydrogeology Journal* (2012) 1–42.
- 786 [9] A. Kemna, B. Kulesa, H. Vereecken, Imaging and characterisation of sub-  
787 surface solute transport using electrical resistivity tomography (ERT) and  
788 equivalent transport models, *Journal of Hydrology* 267 (3) (2002) 125–146.
- 789 [10] K. Singha, S. M. Gorelick, Saline tracer visualized with three-dimensional  
790 electrical resistivity tomography: Field-scale spatial moment analysis, *Wa-*  
791 *ter Resources Research* 41 (5) (2005) W05023.

- 792 [11] D. Pollock, O. A. Cirpka, Fully coupled hydrogeophysical inversion of a  
793 laboratory salt tracer experiment monitored by electrical resistivity tomog-  
794 raphy, *Water Resources Research* 48 (1) (2012) W01505.
- 795 [12] W. Daily, A. Ramirez, D. LaBrecque, J. Nitao, Electrical resistivity tomog-  
796 raphy of vadose water movement, *Water Resources Research* 28 (5) (1992)  
797 1429–1442.
- 798 [13] A. Binley, G. Cassiani, R. Middleton, P. Winship, Vadose zone flow model  
799 parameterisation using cross-borehole radar and resistivity imaging, *Jour-  
800 nal of Hydrology* 267 (3) (2002) 147–159.
- 801 [14] M. C. Looms, K. H. Jensen, A. Binley, L. Nielsen, Monitoring unsaturated  
802 flow and transport using cross-borehole geophysical methods, *Vadose Zone  
803 Journal* 7 (1) (2008) 227–237.
- 804 [15] E. B. Haarder, K. H. Jensen, A. Binley, L. Nielsen, T. Uglebjerg, M. Looms,  
805 Estimation of recharge from long-term monitoring of saline tracer transport  
806 using electrical resistivity tomography, *Vadose Zone Journal* 14 (7) (2015)  
807 1–13.
- 808 [16] W. Menke, *Geophysical Data Analysis: Discrete Inverse Theory*, Interna-  
809 tional Geophysics Series, New York: Academic Press, 1989, Rev. ed. 1.
- 810 [17] S. Friedel, Resolution, stability and efficiency of resistivity tomography  
811 estimated from a generalized inverse approach, *Geophysical Journal Inter-  
812 national* 153 (2) (2003) 305–316.
- 813 [18] F. D. Day-Lewis, K. Singha, A. M. Binley, Applying petrophysical mod-  
814 els to radar travel time and electrical resistivity tomograms: Resolution-  
815 dependent limitations, *Journal of Geophysical Research: Solid Earth*  
816 110 (B8) (2005) B08206.
- 817 [19] K. Singha, S. M. Gorelick, Effects of spatially variable resolution on field-  
818 scale estimates of tracer concentration from electrical inversions using  
819 archies law, *Geophysics* 71 (3) (2006) G83–G91.

- 820 [20] M. Rosas-Carbajal, N. Linde, J. Peacock, F. Zyserman, T. Kalscheuer,  
821 S. Thiel, Probabilistic 3-d time-lapse inversion of magnetotelluric data:  
822 application to an enhanced geothermal system, *Geophysical Journal Inter-*  
823 *national* 203 (3) (2015) 1946–1960.
- 824 [21] J. Doetsch, N. Linde, T. Vogt, A. Binley, A. G. Green, Imaging and quan-  
825 tifying salt-tracer transport in a riparian groundwater system by means of  
826 3D ERT monitoring, *Geophysics* 77 (5) (2012) B207–B218.
- 827 [22] S. C. Constable, R. L. Parker, C. G. Constable, Occam’s inversion: A prac-  
828 tical algorithm for generating smooth models from electromagnetic sound-  
829 ing data, *Geophysics* 52 (3) (1987) 289–300.
- 830 [23] K. Singha, F. D. Day-Lewis, J. Lane, Geoelectrical evidence of bicontinuum  
831 transport in groundwater, *Geophysical Research Letters* 34 (12).
- 832 [24] K. Singha, A. Pidlisecky, F. D. Day-Lewis, M. N. Gooseff, Electrical charac-  
833 terization of non-fickian transport in groundwater and hyporheic systems,  
834 *Water Resources Research* 44 (4) (2008) W00D07.
- 835 [25] R. D. Swanson, A. Binley, K. Keating, S. France, G. Osterman, F. D. Day-  
836 Lewis, K. Singha, Anomalous solute transport in saturated porous media:  
837 Relating transport model parameters to electrical and nuclear magnetic  
838 resonance properties, *Water Resources Research* 51 (2) (2015) 1264–1283.
- 839 [26] M. A. Briggs, F. D. Day-Lewis, J. B. Ong, G. P. Curtis, J. W. Lane, Si-  
840 multaneous estimation of local-scale and flow path-scale dual-domain mass  
841 transfer parameters using geoelectrical monitoring, *Water Resources Re-*  
842 *search* 49 (9) (2013) 5615–5630.
- 843 [27] M. A. Briggs, F. D. Day-Lewis, J. B. Ong, J. W. Harvey, J. W. Lane,  
844 Dual-domain mass-transfer parameters from electrical hysteresis: Theory  
845 and analytical approach applied to laboratory, synthetic streambed, and  
846 groundwater experiments, *Water Resources Research* 50 (10) (2014) 8281–  
847 8299.

- 848 [28] F. D. Day-Lewis, N. Linde, R. Haggerty, K. Singha, M. A. Briggs, Pore  
849 network modeling of the electrical signature of solute transport in dual-  
850 domain media, *Geophysical Research Letters* 44 (10) (2017) 4908–4916,  
851 2017GL073326.
- 852 [29] R. Glass, M. Nicholl, Physics of gravity fingering of immiscible fluids within  
853 porous media: An overview of current understanding and selected compli-  
854 cating factors, *Geoderma* 70 (2-4) (1996) 133–163.
- 855 [30] Y. Méheust, G. Løvoll, K. J. Måløy, J. Schmittbuhl, Interface scaling in  
856 a two-dimensional porous medium under combined viscous, gravity, and  
857 capillary effects, *Physical Review E* 66 (5) (2002) 051603.
- 858 [31] R. Toussaint, K. J. Måløy, K., Y. Méheust, G. Løvoll, M. Jankov,  
859 G. Schäfer, J. Schmittbuhl, Two-phase flow: structure, upscaling, and  
860 consequences for macroscopic transport properties, *Vadose Zone Journal*  
861 11 (3).
- 862 [32] A. Ferrari, I. Lunati, Direct numerical simulations of interface dynamics  
863 to link capillary pressure and total surface energy, *Advances in Water Re-*  
864 *sources* 57 (2013) 19–31.
- 865 [33] G. Løvoll, M. Jankov, K. J. Måløy, R. Toussaint, J. Schmittbuhl,  
866 G. Schäfer, Y. Méheust, Influence of viscous fingering on dynamic  
867 saturation-pressure curves in porous media, *Transport in Porous Media*  
868 86 (2011) 305–324.
- 869 [34] S. M. Hassanizadeh, M. A. Celia, H. K. Dahle, Dynamic effect in the capil-  
870 lary pressure–saturation relationship and its impacts on unsaturated flow,  
871 *Vadose Zone Journal* 1 (1) (2002) 38–57.
- 872 [35] J. Jiménez-Martínez, P. de Anna, H. Tabuteau, R. Turuban, T. L. Borgne,  
873 Y. Méheust, Pore-scale mechanisms for the enhancement of mixing in un-  
874 saturated porous media and implications for chemical reactions, *Geophys-*  
875 *ical Research Letters* 42 (13) (2015) 5316–5324.

- 876 [36] J. Jiménez-Martínez, T. Le Borgne, H. Tabuteau, Y. Méheust, Impact of  
877 saturation on dispersion and mixing in porous media: Photobleaching pulse  
878 injection experiments and shear-enhanced mixing model, *Water Resources*  
879 *Research* 53 (2017) 1457–1472.
- 880 [37] M. Dentz, T. Le Borgne, A. Englert, B. Bijeljic, Mixing, spreading and  
881 reaction in heterogeneous media: A brief review, *Journal of Contaminant*  
882 *Hydrology* 120 (2011) 1–17.
- 883 [38] T. Le Borgne, M. Dentz, P. Davy, D. Bolster, J. Carrera, J.-R. De Dreuzy,  
884 O. Bour, Persistence of incomplete mixing: A key to anomalous transport,  
885 *Physical Review E* 84 (1) (2011) 015301.
- 886 [39] M. Seyfried, P. Rao, Solute transport in undisturbed columns of an aggre-  
887 gated tropical soil: Preferential flow effects, *Soil Science Society of America*  
888 *Journal* 51 (6) (1987) 1434–1444.
- 889 [40] J. Koestel, M. Larsbo, Imaging and quantification of preferential solute  
890 transport in soil macropores, *Water Resources Research* 50 (5) (2014) 4357–  
891 4378.
- 892 [41] T. W. Willingham, C. J. Werth, A. J. Valocchi, Evaluation of the effects  
893 of porous media structure on mixing-controlled reactions using pore-scale  
894 modeling and micromodel experiments, *Environmental science & technol-*  
895 *ogy* 42 (9) (2008) 3185–3193.
- 896 [42] P. de Anna, J. Jimenez-Martinez, H. Tabuteau, R. Turuban, T. Le Borgne,  
897 M. Derrien, Y. Méheust, Mixing and reaction kinetics in porous media: An  
898 experimental pore scale quantification, *Environmental Science & Technol-*  
899 *ogy* 48 (1) (2013) 508–516.
- 900 [43] B. Kozlov, M. Schneider, B. Montaron, M. Lagues, P. Tabeling, Archie's  
901 law in microsystems, *Transport in Porous Media* (2012) 1–20.

- 902 [44] A. Ferrari, J. Jimenez-Martinez, T. L. Borgne, Y. Méheust, I. Lunati, Chal-  
903 lenges in modeling unstable two-phase flow experiments in porous micro-  
904 models, *Water Resources Research* 51 (3) (2015) 1381–1400.
- 905 [45] R. Sjöback, J. Nygren, M. Kubista, Absorption and fluorescence properties  
906 of fluorescein, *Spectrochimica Acta Part A: Molecular and Biomolecular*  
907 *Spectroscopy* 51 (6) (1995) L7–L21.
- 908 [46] C. Schlumberger, *Etude sur la prospection électrique du sous-sol* [Study on  
909 underground electrical prospecting], Gauthier-Villars, 1920.
- 910 [47] D. Jougnot, A. Ghorbani, A. Revil, P. Leroy, P. Cosenza, Spectral in-  
911 duced polarization of partially saturated clay-rocks: A mechanistic ap-  
912 proach, *Geophysical Journal International* 180 (1) (2010) 210–224.
- 913 [48] K. T. Tallakstad, H. A. Knudsen, T. Ramstad, G. Løvoll, K. J. Måløy,  
914 R. Toussaint, E. G. Flekkøy, Steady-State Two-Phase Flow in Porous  
915 Media: Statistics and Transport Properties, *Physical Review Letters* 102  
916 (2009) 074502.
- 917 [49] R. Künze, I. Lunati, An adaptive multiscale method for density-driven  
918 instabilities, *Journal of Computational Physics* 231 (17) (2012) 5557–5570.
- 919 [50] G. Archie, The electrical resistivity log as an aid in determining some reser-  
920 voir characteristics, *Transaction of the American Institute of Mining and*  
921 *Metallurgical Engineers* 146 (1942) 54–61.
- 922 [51] S. P. Friedman, Soil properties influencing apparent electrical conductivity:  
923 a review, *Computers and electronics in agriculture* 46 (1) (2005) 45–70.
- 924 [52] M. Caceci, W. Cacheris, Simplex optimization algorithm, *Byte* 5 (1984)  
925 340–351.
- 926 [53] O. Wiener, Theory of composite bodies, *Abh. sächs. Ges. Wiss.* 33 (1912)  
927 507–525.

- 928 [54] A. Maineult, D. Jougnot, A. Revil, Variations of petrophysical properties  
929 and spectral induced polarization in response to drainage and imbibition:  
930 a study on a correlated random tube network, submitted to Geophysical  
931 Journal International.
- 932 [55] A. Revil, D. Jougnot, Diffusion of ions in unsaturated porous materials,  
933 Journal of Colloid and Interface Science 319 (1) (2008) 226–235.
- 934 [56] D. Jougnot, A. Revil, P. Leroy, Diffusion of ionic tracers in the callovo-  
935 oxfordian clay-rock using the donnan equilibrium model and the formation  
936 factor, *Geochimica et Cosmochimica Acta* 73 (10) (2009) 2712–2726.
- 937 [57] S. Hamamoto, P. Moldrup, K. Kawamoto, T. Komatsu, Excluded-volume  
938 expansion of Archie’s law for gas and solute diffusivities and electrical  
939 and thermal conductivities in variably saturated porous media, *Water Re-*  
940 *sources Research* 46 (6).
- 941 [58] A. Revil, Thermal conductivity of unconsolidated sediments with geophys-  
942 ical applications, *Journal of Geophysical Research* 105 (B7) (2000) 16749–  
943 16.
- 944 [59] D. Jougnot, A. Revil, et al., Thermal conductivity of unsaturated clay-  
945 rocks, *Hydrology and Earth System Sciences* 14 (1) (2010) 91–98.
- 946 [60] R. Hill, Elastic properties of reinforced solids: Some theoretical principles,  
947 *Journal of the Mechanics and Physics of Solids* 11 (5) (1963) 357 – 372.
- 948 [61] V. Joekar-Niasar, S. M. Hassanizadeh, Specific interfacial area: The missing  
949 state variable in two-phase flow equations?, *Water Resources Research* 47  
950 (2011) W05513.
- 951 [62] N. Linde, L. B. Pedersen, Evidence of electrical anisotropy in limestone  
952 formations using the RMT technique, *Geophysics* 69 (4) (2004) 909–916.
- 953 [63] D. J. LaBrecque, D. Casale, Experience with anisotropic inversion for elec-  
954 trical resistivity tomography, in: 15th EEGS Symposium on the Applica-  
955 tion of Geophysics to Engineering and Environmental Problems, 2002.

- <sup>956</sup> [64] C. C. Pain, J. V. Herwanger, J. H. Saunders, M. H. Worthington, C. R.  
<sup>957</sup> de Oliveira, Anisotropic resistivity inversion, *Inverse Problems* 19 (5) (2003)  
<sup>958</sup> 1081.

ACCEPTED MANUSCRIPT

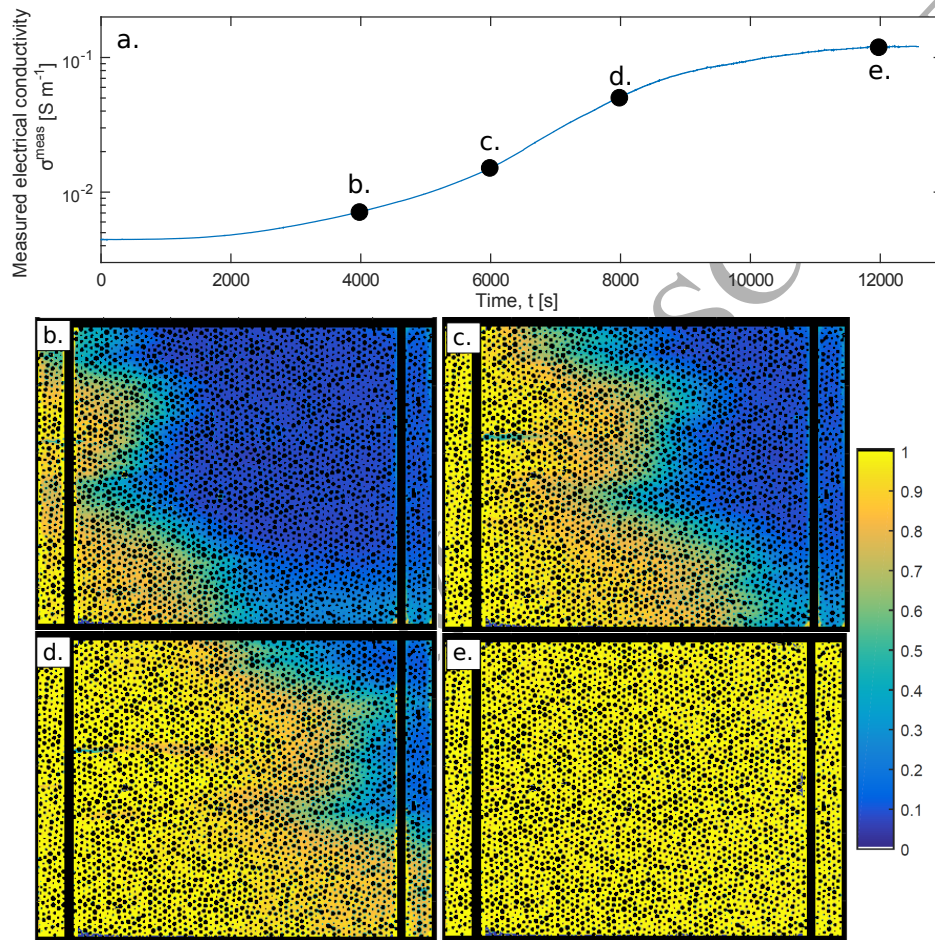


Figure 5: (a) Measured effective bulk electrical conductivity as a function of the time since the initiation of a tracer test in saturated conditions and corresponding images of the normalized tracer concentration in the flow cell at (b)  $t = 4000$  s, (c)  $t = 6000$  s, (d)  $t = 8000$  s, and (e)  $t = 12000$  s. The grains, the top and bottom boundaries, and the four electrodes appear as either black lines or circles on the image.

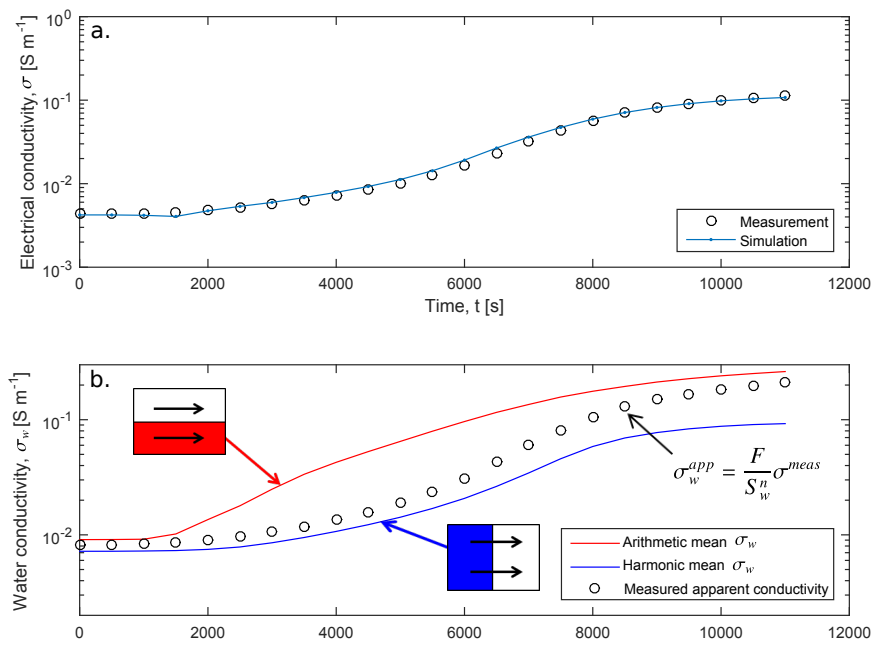


Figure 6: (a) Comparison between measured and simulated electrical conductivities at the scale of the flow cell under saturated conditions ( $RMSE = 0.0021 \text{ S m}^{-1}$ ). (b) Apparent water electrical conductivity from Eq. 2 (with  $F = 1.85$ ) and Wiener bound values of the wetting phase at the flow cell scale.

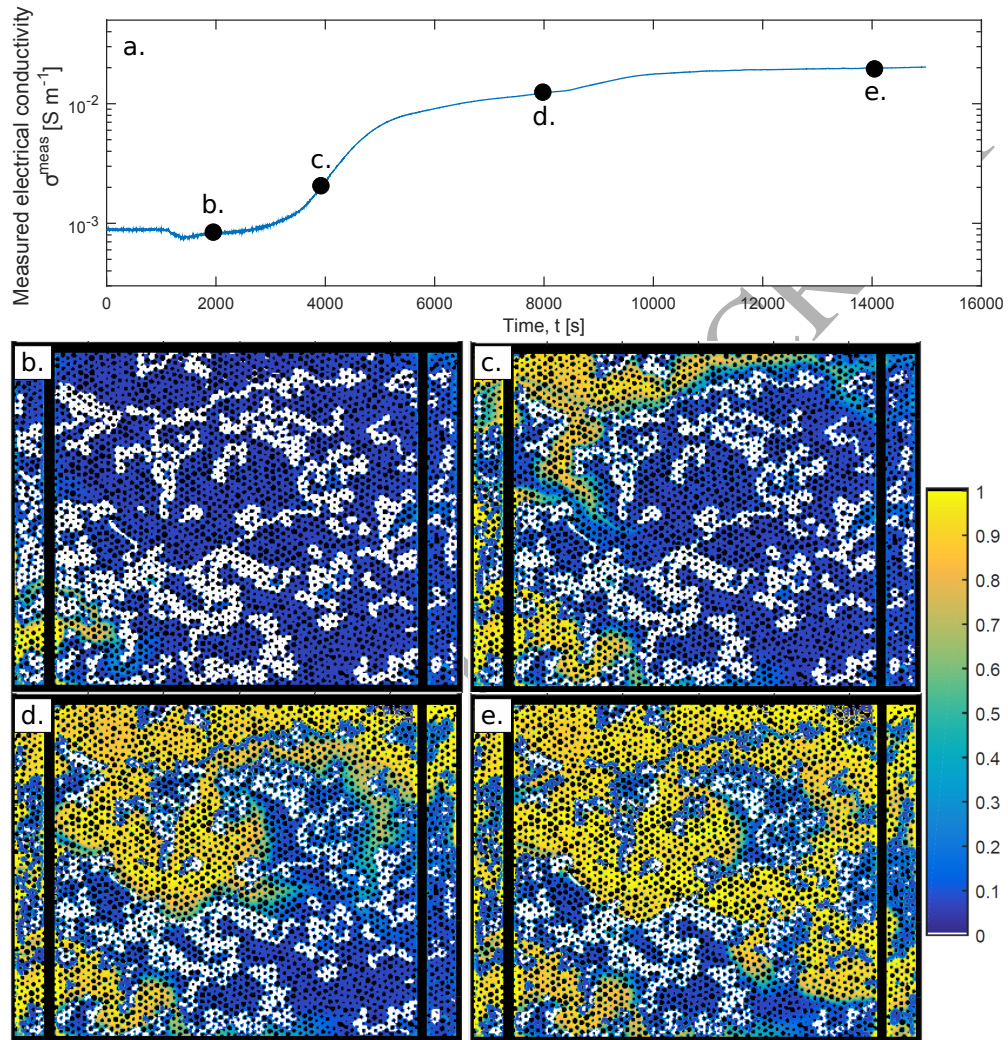


Figure 7: (a) Measured effective bulk electrical conductivity as a function of the time during a tracer test in partially saturated conditions and corresponding images of the normalized tracer concentration in the test cell at (b)  $t = 2000$  s, (c)  $t = 4000$  s, (d)  $t = 8000$  s, and (e)  $t = 14000$  s. The grains, the top and bottom boundaries, and the four electrodes appear as either black lines or circles on the image. The air appears in white clusters since there is no fluorescein in this phase. During the course of the experiment, the water saturation increased from  $S_w = 0.69$  to  $0.87$ .

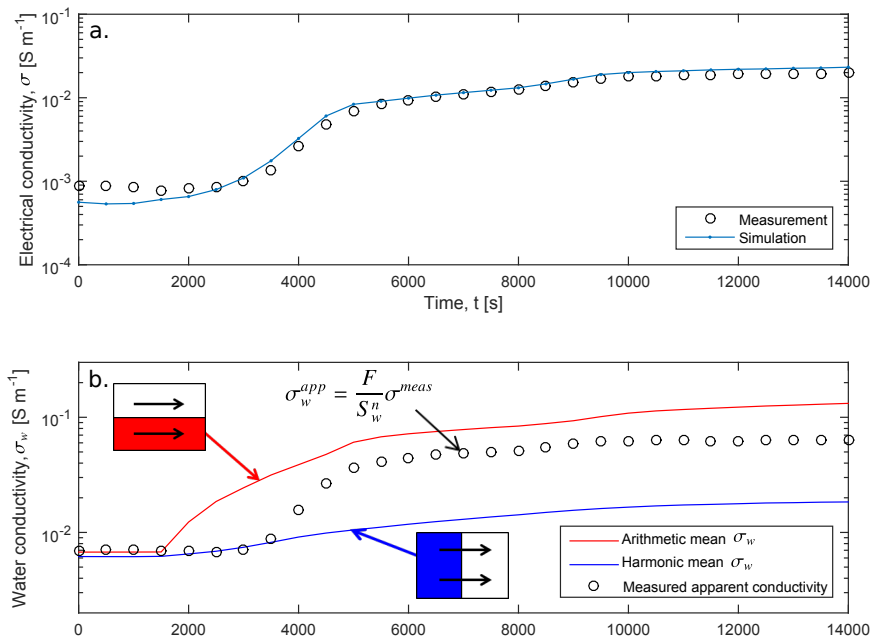


Figure 8: (a) Comparison between measured and simulated electrical conductivities at the scale of the flow cell under partially saturated conditions ( $RMSE = 0.0017 \text{ S m}^{-1}$ ). (b) Apparent water electrical conductivity from Eq. 2 (with  $F = 1.85$  and  $n = 4$ ) and Wiener bound values of the wetting phase at the flow cell's scale. Note that the water saturation increased from  $S_w = 0.69$  to  $0.87$  during the test.

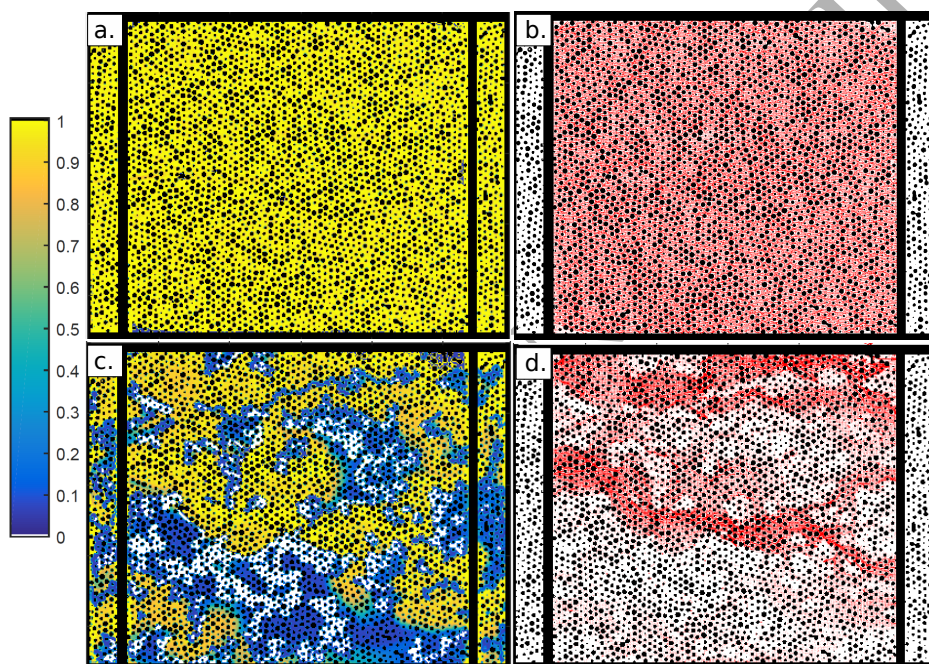


Figure 9: (a and c) Normalized tracer concentration and (b and d) current density spatial distribution at a late stage of the tracer test experiments under saturated (a and b correspond to  $t = 12000$  s) and partially saturated (c and d correspond to  $t = 14000$  s) conditions. Note that we only display the current density as red streamline density between P1 and P2, masking the effect of the high conductivity of the copper electrode to improve the readability of Figs. 9b and d.

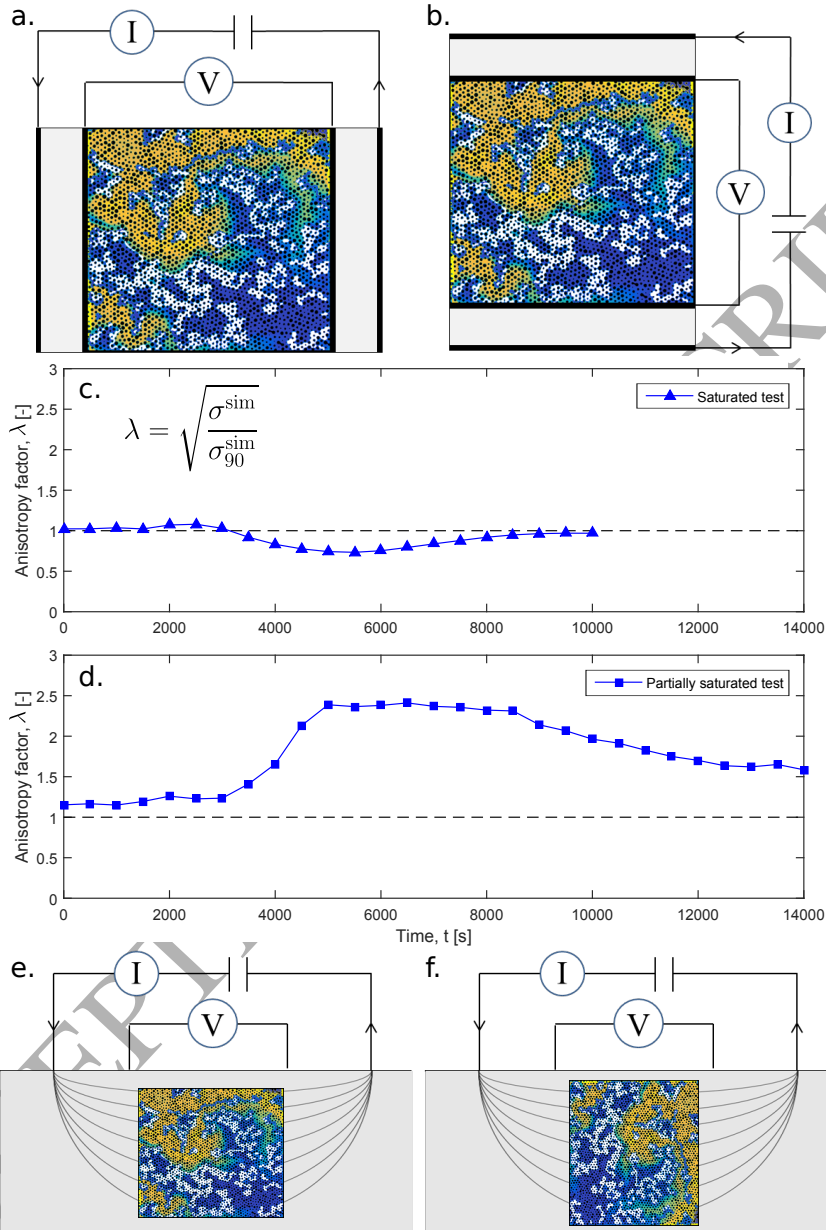


Figure 10: Numerical study of anisotropy in the effective bulk electrical conductivity during tracer experiments for (a) the experimental configuration with longitudinal electrical transport and (b) a rotation of the set of electrodes with respect to the medium by  $90^\circ$  (i.e., imposing transverse electrical transport with respect to the main flow direction). (c) The electrical anisotropy factor as a function of time during the saturated tracer test. (d) Same as (c) for partially saturated conditions. Note that the anisotropy study is only conducted on the part of the cell between P1 and P2 (i.e., the investigation zone). The dashed line corresponds to the value  $\lambda = 1$ . Conceptual view of surface-based ERT measurements for (e) lateral and (f) vertical tracer flow in the near surface.